

Comparison of Compound Lean Nozzles and Controlled Flow Nozzles at Off-Design

Jani Keränen

Lappeenranta University of Technology
Department of Energy and Environmental Technology

Comparison of Compound Lean Nozzles and Controlled Flow Nozzles at Off-Design

The topic of the Thesis has been confirmed by
the Departmental Council on 4th April 2003

Examiners: Prof. Dr. Jari Backman
Prof. Dr. Hermann Haselbacher

Lappeenranta 30th October 2003

Jani Keränen

Tapolantie 262
FIN-47490 MANKALA
+358 405877904

TIIVISTELMÄ

Lappeenrannan Teknillinen Yliopisto
Energia- ja ympäristötekniikan osasto

Jani Keränen

Comparison of Compound Lean Nozzles and Controlled Flow Nozzles at Off-Design

Diplomityö

2003

63 sivua, 28 kuvaa, 6 taulukkoa ja 1 liite.

Tarkastajat: Prof. TkT. Jari Backman
Prof. TkT. Hermann Haselbacher

Hakusanat: Aksiaaliturbiini, suutin, laskennallinen virtausmekaniikka.

Turbokoneet ja etenkin höyryturbiinit ovat usein suunniteltu ja optimoitu toimimaan tietyssä toimintapisteessä jossa häviöt on minimoitu ja hyötysuhde maksimoitu. Joissakin tapauksissa on kuitenkin tarpeellista käyttää turbiinia toimintapisteiden ulkopuolella. Tällöin turbiinin läpi virtaava massavirta muuttuu ja yleensä heikentää hyötysuhdetta.

Turbokoneiden suorituskykyä voidaan parantaa käyttämällä kolmidimensionaalisesti muotoiltuja siipiä. Työssä on vertailtu laskennallisesti kahta kohtuullisesti muotoiltua suutinta (Compound lean ja Controlled flow) niiden suunnitellun toimintapisteiden ulkopuolella. Kolmas suutin, ilman kolmidimensionaalista muotoilua on mukana vertailukohteena.

Suutinten suorituskykyä tutkitaan laskennallisen virtausmekaniikan avulla olosuhteissa, jotka ovat toimintapisteiden ulkopuolella. Virtauksen muutoksia tutkitaan kokonaispainehäviön, isentrooppisen hyötysuhteen ja virtauspinnan yhdenmukaisuuden avulla. Virtauspintoja verrataan ulosvirtauskulman, massavirran ja toisiovirtausvektoreiden jakauman avulla.

Erot suutinten suorituskykyssä korostavat ylikuormalla. Kun massavirran arvoa on kohotettu eniten, Compound lean suuttimilla hyötysuhde laskee Controlled flow suuttimeen verrattuna vähemmän. Alikuormalla, kun massavirran arvoa lasketaan, erot suuttimien suorituskyvyssä pienenevät ja tutkittujen suuttimien ulosvirtaus on samankaltainen.

ABSTRACT

Lappeenranta University of Technology
Department of Energy and Environmental Technology

Jani Keränen

Comparison of Compound Lean Nozzles and Controlled Flow Nozzles at Off-Design

Thesis for the Degree of Master of Science in Technology

2003

63 pages, 28 figures, 6 tables and 1 appendix.

Examiners: Proff. Dr. Jari Backman
Proff. Dr. Hermann Haselbacher

Keywords: Axial flow turbine, compound lean nozzles, controlled
flow nozzles, computational fluid dynamics, off-design.

Turbomachines like steam turbines are often designed and optimized for a specific load, where the losses are minimized and efficiency is maximized. On some instances, it is necessary to operate a turbine at different conditions as it was designed for, in so called off-design conditions. This causes changes in massflow through the turbine, resulting usually in a lowered efficiency.

The performance of turbomachines can be improved by the application of three-dimensionally shaped bladings. In the study two moderately shaped nozzles, compound lean nozzles and controlled flow nozzles, are compared numerically in the conditions reflecting to out of nominal operating point. A third nozzle, without three-dimensional shaping, is included to serve as a reference.

The performance of the nozzles at off-design conditions is studied by the means of Computational Fluid Dynamics (CFD). The changes in the flow are investigated in respect to total pressure losses, isentropic efficiency and flow field homogeneity. The flow fields are compared with distributions of outlet flow angle, massflow and secondary velocity vectors.

The differences of the nozzles performances are highlighted at high overload, where the massflow was increased the most. The compound lean nozzles performed with a less drop in efficiency as the controlled flow nozzles. At part load, at lower massflow, the differences of the nozzle's performance become smaller and the outflows of the investigated nozzles are similar to each other.

Contents

Nomeclature

Acknowledgements

Introduction

1	Geometries	1
1.1	Original geometry	1
1.1.1	ERCOFTAC test-case	1
1.1.2	Annular cascade	1
1.1.3	Profile	1
1.2	From annular to linear cascade	2
1.2.1	Linear cascade	3
1.2.2	Used geometries	3
1.2.3	Coordinate system	3
1.2.4	Cylindrical nozzles	4
1.2.5	Compound lean nozzles	4
1.2.6	Controlled flow nozzles	7
2	Modelling	11
2.1	Off-Design	11
2.2	Governing equations of the fluid flow	14
2.3	Fully compressible flow	15
2.4	Turbulence	15
2.4.1	Variables defining the turbulence	16

2.4.2	Turbulence model	17
2.4.3	Fluid properties	18
2.5	Boundary conditions	19
2.5.1	Inlet	19
2.5.2	Walls	21
2.5.3	Outlet	21
2.5.4	Symmetry	21
2.5.5	Periodicity	21
2.6	Mesh	22
2.6.1	Cylindrical nozzles	25
2.6.2	Compound lean nozzles	25
2.6.3	Controlled flow nozzles	26
2.7	Solver	28
2.7.1	Finite Volume method	28
2.7.2	Data export	29
2.7.3	Post-processing	30
3	Secondary flow and losses	31
3.1	Secondary flow	31
3.1.1	Secondary flow and vorticity	31
3.1.2	Influences of the secondary flow	33
3.2	Losses	34
3.2.1	Loss generation	34
3.2.2	Secondary losses	35
3.2.3	Profile losses	36
4	Results of the CFD	37
4.1	Secondary velocities	37
4.1.1	Calculation of the secondary velocity vectors	37
4.1.2	Secondary velocity vector plots	39
4.1.3	Identification of the vortices	40

4.1.4	Secondary flow at off-design	46
4.2	Mass flow density	47
4.3	Inhomogeneity of the outlet flow field	49
4.4	Outlet flow angle	50
4.5	The total pressure loss	52
4.5.1	Spanwise distribution of the total pressure losses	53
4.5.2	Total pressure loss countours	54
4.6	Isentropic efficiency	55
4.7	Comparison of the results with measurements	56
5	Conclusions and discussion	58
5.1	Losses	58
5.2	Inhomogeneity of the outlet flow field	59
5.3	Secondary flow and vortices	59
5.4	Massflow density	59
5.5	Isentropic efficiency	59
5.6	Summary	60
	Bibliography	61
	Appendix A	

Nomenclature

Latin symbols

a	parameter	m
a	throat width	m
A	area	m^2
c	chord length	m
c	absolute velocity	m/s
C	constant	-
c_p	specific heat capacity	J/kgK
c_v	specific heat capacity	J/kgK
D_{Hub}	hub diameter	m
D_M	distance of the blade midspan from the center of the axis	m
D_{Tip}	tip diameter	m
h	blade span	m
h	static (thermodynamic) enthalpy	J/kg
h_s	isentropic enthalpy	J/kg
H	total enthalpy	J/kg
I	turbulence intensity	-
k	turbulent kinetic energy	J
K_{irr}	irreversibly averaged kinetic energy	J
K_{rev}	reversibly averaged kinetic energy	J
l_t	dissipation length scale	m
M	molecular weight	kg/kmol
p	pressure	Pa
P	production rate	-
P_s	shear part of the production	-
r	radius	m

R	radius of the rotor	m
R	universal gas constant	J/kmolK
s	spacing	m
s/c	pitch/chord ratio	-
T	temperature	K
u	circumferential velocity	m/s
u_τ	friction speed	m/s
v	circumferential velocity component	m/s
w	relative velocity	m/s
w	spanwise velocity	m/s
Y	coordinates in the geometry modification	-
y^+	dimensionless wall distance	-

Greek symbols

α	flow angle	deg
β	stagger angle, constant	deg
ΔK	inhomogeneity	J/kg
$\dot{Q}_{m,i}$	mass flow density	kgm ²
ϵ	turbulent energy dissipation rate	-
η_0	constant	-
κ	ratio of the specific heat capacities c_p/c_v	-
λ	thermal conductivity	J/msK
μ	molecular laminar viscosity	kg/ms
μ_T	turbulent dynamic viscosity	kg/ms
ν	kinematic viscosity	m ² /s
ω	rotational speed, total pressure loss coefficient	rad/s, -
ϕ	lean angle	deg
ϕ	flow coefficient	-
ρ	density	kg/m ³
σ_ϵ	constant	-
σ_k	constant	-
τ_{ij}	stress tensor	N/m ²
ξ	loss	-

Subscripts

DP	design-point
p	pitchwise averaged values, profile
prim	primary
pro	projected
ref	reference
sec	secondary
tot	total
x	axial
y	circumferential
z	spanwise

Superscripts

'	fluctuating component
---	-----------------------

Abbreviations

CFD	Computational Fluid Dynamics
CFN	Controlled Flow Nozzles
CLN	Compound Lean Nozzles
CYL	Cylindrical Nozzles
RNG	Renormalization Group

Acknowledgements

I would like to express my gratitude to my supervisor, professor Dr. Jari Backman for his supervision and guidance in this thesis.

I would like to express my gratitude also to my supervisor, professor Dr. Hermann Haselbacher for the opportunity to conclude this thesis at the institute for Thermal Turbomachines and Powerplants in the Vienna University of Technology and for his supervision and support during the work.

I would like to express my gratitude to Dr. Franz Wingelhofer for the technical support and valuable guidance through out the research.

I would like to thank the Austrian Exchange Service (ÖAD) and the Fortum Foundation for their financial support during the thesis project.

I would also like to thank my family and friends for their support during the thesis. Finally, I would like to thank Birgit, for her love and care while I performed this thesis.

Introduction

A turbine blade row is usually designed to produce minimum losses at its design operating point. When the operating point of the turbine is changed, additional losses occur which result in a reduced efficiency. The studied moderately three-dimensionally shaped nozzle bladings differ from their approach to provide the highest efficiency at the design operating point. Therefore, a different performance the nozzles at off-design conditions may be expected.

Numerous studies have been concluded for the optimization at design point conditions, for the controlled flow nozzles geometry and for the compound lean nozzles. There exists as well several studies for turbine cascades about the effect of the incidence angle reflecting to off-design conditions. However, a comparison of these two widely used nozzle's geometries at off-design operating conditions is not available in the open literature.

The geometries for compound lean nozzles and controlled flow nozzles have been optimized in a previous work concluded at the Institute of Thermal Turbomachines and Powerplants at Vienna University of Technology. Further details of the optimization of the geometries can be found from the work of Schiebenes (2001).

The changes in the operating point affect the incidence angle and the mass-flow. In this study, these changes are expressed together by the means of the flow coefficient, defined as ratio of the axial velocity component and circumferential velocity. The flow coefficient, defined at the inlet of the cascade, is altered with 75, 85, 115 and 125 percent of its design operating point value.

In the work, a description for the construction of this nozzles used in the study is provided. The numerical methods used for the simulations are pre-

sented. The obtained results are discussed in detail and a summary of them is provided. The aim of the work is to provide objective comparison of compound lean nozzles and controlled flow nozzles in amount of the nominal operation point conditions.

Chapter 1

Geometries

1.1 Original geometry

1.1.1 ERCOFTAC test-case

Profile for the stator blades was obtained from the Von Karman Institute ERCOFTAC test-case 6 (TSIG U1). The test-case is a 1-1/2 stage axial flow cold air turbine, with two stator rows and one rotor row. More information about the test-case can be found from the work of Walraevens (1990).

1.1.2 Annular cascade

The original geometry was for an annular cascade with radially stacked stator blades. The geometrical data of the stator cascade used in the test-case are collected in table 1.1.

1.1.3 Profile

The stator profile is untwisted and all cross sections have a constant inner and outer diameter. The stator profile of the test-case is a Traupel profile, illustrated in figure 1.1.

Table 1.1: *Geometrical data of the annular stator cascade.*

Tip diameter	D_{Tip}	600.0 mm
Hub diameter	D_{Hub}	490.0 mm
Blade span	h	55.0 mm
Number of the blades	N	36
Chord	c	62.0 mm
Pitch/chord ratio	s/c	0.767
Aspect ratio	h/c	0.887
Inlet flow angle *	α_0	90 °
Outlet flow angle *	α_1	20 °

(* with respect to the circumferential direction)

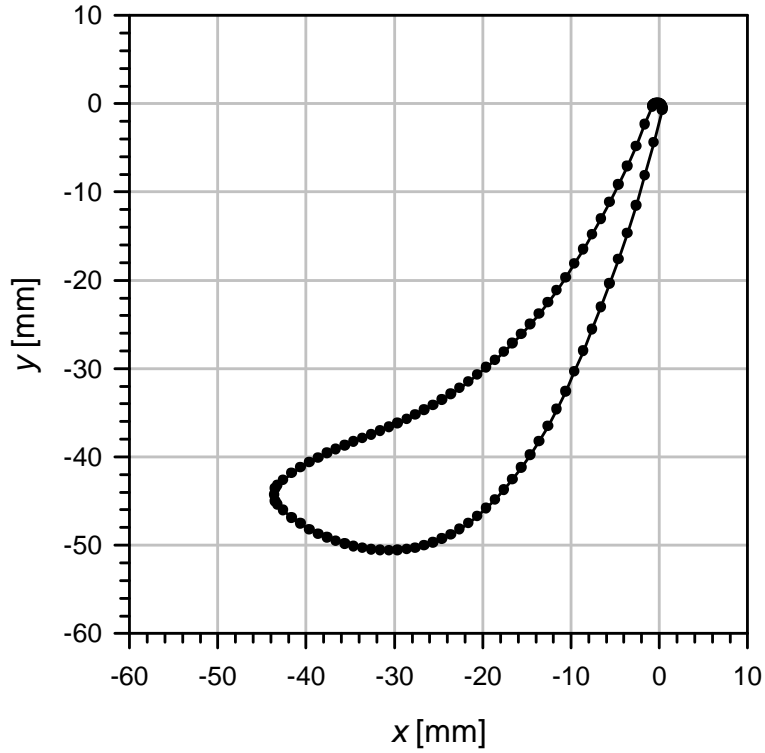


Fig. 1.1: *Stator Traupel profile from the ERCOFTAC test-case 6*

1.2 From annular to linear cascade

For the computational modelling the original annular cascade is simplified to a linear cascade. This is done in order to reduce the computational domain. As in the linear cascade the geometry is symmetrical over the midspan, it is sufficient to model only half of it in the spanwise direction. Therefore, the

grid generation simplifies and the number of the cells is reduced to half.

1.2.1 Linear cascade

While transforming the annular cascade to a linear one, the spacing s becomes constant over span. The spacing is determined as the mean spacing for the annular cascade:

$$D_M = \sqrt{0,5 \cdot (D_{Tip}^2 + D_{Hub}^2)} = 547.8mm \quad (1.1)$$

$$s = \frac{D_M \cdot \pi}{N} = 47.8mm \quad (1.2)$$

where D_M is the distance of the blade midspan from axis of rotation.

1.2.2 Used geometries

Three different blade geometries are used in this work: *cylindrical nozzles*, *compound lean nozzles* and *controlled flow nozzles*. The cylindrical nozzles are used as reference for the two modified nozzles. The blades, used to construct the compound lean nozzles, are created by leaning the blades spanwisely in pitchwise direction. For the controlled flow nozzles the blades are constructed by twisting the blade about the trailing edge.

1.2.3 Coordinate system

A cartesian coordinate system is used. The origin is located at the trailing edge of the blade, in the midspan section. The x -axis points in axial direction of the turbine, increasing in the flow direction. The y -axis points in pitchwise direction, from pressure side to the suction side. The x - and y -axis are illustrated in figure 1.1. The z -axis points in the spanwise direction, with the origin at the midspan.

1.2.4 Cylindrical nozzles

The cylindrical nozzles are created by extruding the original Traupel profile (illustrated in figure 1.1) in spanwise direction. An example of the cylindrical blade is illustrated in figure 1.2.

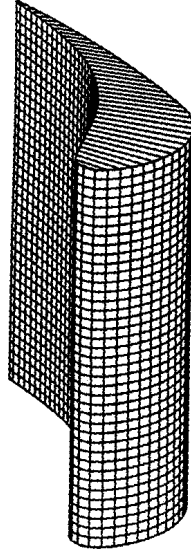


Fig. 1.2: *Example of a cylindrical blade (Haller, 1997)*

1.2.5 Compound lean nozzles

The *Compound Lean* design is based on the pitchwise leaning of the fixed profiles, resulting into "banana" shaped blades. The geometry was optimized in the work of Schiebenes (2001).

The positive lean introduces higher pressure in the endwall regions compared to midspan. Resulting in lower velocities in the endwall regions. This decreases loading at the hub and at the tip and increases loading in the midspan region. This reduces secondary loss generation. The higher pressure in the endwall regions also increases the movement of the low energy fluid from endwalls towards midspan, which results in a more developed secondary flow. Harrison (1989) found that the overall losses of a cascade with cylindrical nozzles do not differ from the overall losses with compound leaned nozzles considerably. He gave reasons for this by the spanwise movement of the low energy fluid. The losses are moved from the endwalls closer to midspan. An example of a compound lean blade is illustrated in figure 1.3.

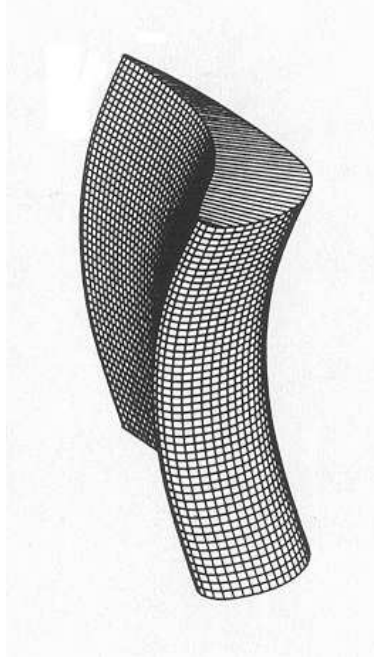


Fig. 1.3: *Example of an compound lean blade (Haller, 1997)*

Construction of the geometry

A positive compound lean blade has a concave suction side and a convex pressure side. A typical blade is illustrated in figure 1.3. The blade is formed of the cylindrical blade by spanwise leaning in the pitchwise direction. Practically, this is done by shifting the whole mesh in the pitchwise direction, with respect to the spanwise distance from the wall. The shift in the pitchwise direction ΔY follows a parabolic form and can be written as

$$\Delta Y \left(\frac{z}{h} \right) = a_0 + a_1 \left(\frac{z}{h} \right) + a_2 \left(\frac{z}{h} \right)^2. \quad (1.3)$$

According to symmetry, parameter a_1 is 0. The profiles at the endwalls are not shifted pitchwisely, leading to

$$\Delta Y \left(\frac{z}{h} = \pm 1/2 \right) = 0 \quad (1.4)$$

$$\implies a_0 = -\frac{a_2}{4} \quad (1.5)$$

and equation 1.3 becomes

$$\Delta Y \left(\frac{z}{h} \right) = a_2 \left[\left(\frac{z}{h} \right)^2 - \frac{a_2}{4} \right]. \quad (1.6)$$

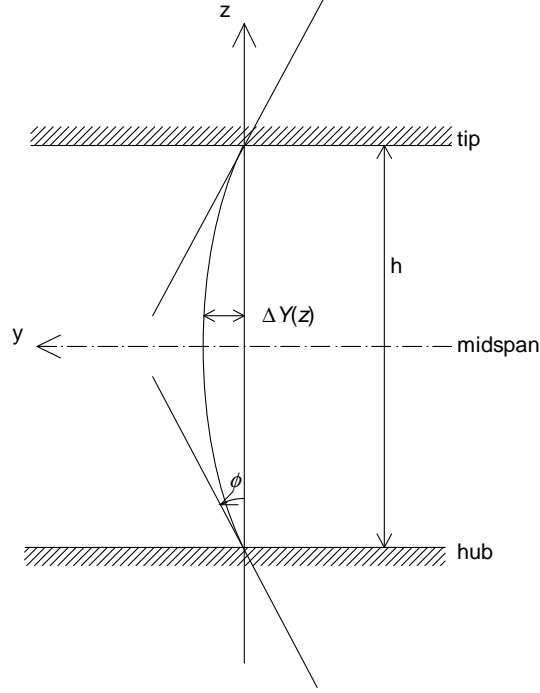


Fig. 1.4: *Abbreviations used in calculation of the leaning*

In order to express the magnitude of the leaning, a lean angle ϕ is defined at the hub

$$\Delta Y \left(\frac{z}{h} \right) = -\tan \phi. \quad (1.7)$$

The angle ϕ is illustrated in figure 1.4. The optimum lean angle is 10° (Schiebenes, 2001). Equation 1.7 combined with the derivation of equation 1.6 at $\left(\frac{z}{h} = -1/2 \right)$ gives the parameter a_2

$$a_2 = -\tan \phi, \quad (1.8)$$

Finally, equation 1.6 becomes

$$\Delta Y \left(\frac{z}{h} \right) = \tan \phi \left[\frac{1}{4} - \left(\frac{z}{h} \right)^2 \right]. \quad (1.9)$$

1.2.6 Controlled flow nozzles

Controlled flow blades are formed by twisting the blade sections so that, compared to midspan, the throat openings are reduced at the endwalls of the blade row. In this work, a spanwise parabolic form of the variation in the stagger angle is used.

This arrangement reduces the massflow near the endwall regions of the nozzles and increases it in the midspan region. This reduces the secondary losses, introduced in the vicinity of the endwalls. An example of a controlled flow blade is illustrated in figure 1.5.

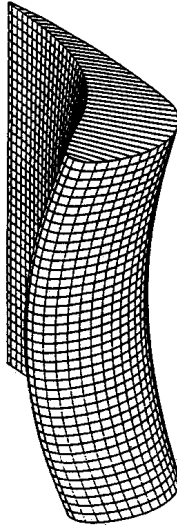


Fig. 1.5: *Example of a controlled flow blade (Haller, 1997).*

Construction of the geometry

The controlled flow blades are constructed by rotating the profiles at the trailing edges. This results in variable stagger angles in the spanwise direction. Since the trailing edges are kept straight in the spanwise direction, the throat opening of the nozzles changes. The change in the stagger angle is set to be parabolic in the spanwise direction:

$$\Delta\beta\left(\frac{z}{h}\right) = a_0 + a_1\left(\frac{z}{h}\right) + a_2\left(\frac{z}{h}\right)^2 \quad (1.10)$$

For the $\frac{z}{h} = 0$, parameter a_0 becomes the change of the stagger angle at midspan $\Delta\beta_M$. Due to symmetry with respect to midspan, parameter a_1 becomes 0. Thus, parameter a_2 can be expressed at the endwall ($\frac{z}{h} = \pm\frac{1}{2}$):

$$a_2 = 4(\Delta\beta_W - \Delta\beta_M). \quad (1.11)$$

Where index W refers to the endwalls. Now equation (1.10) can be written as

$$\Delta\beta\left(\frac{z}{h}\right) = \Delta\beta_M + 4(\Delta\beta_W - \Delta\beta_M)\left(\frac{z}{h}\right)^2. \quad (1.12)$$

This equation will result in convex pressure sides and concave suction sides, if $\Delta\beta_M < \Delta\beta_W$. As the change of the stagger angle at midspan will be chosen, it is necessary to find a relation between the change of the stagger angle at midspan and the endwalls. For that, the specific work a_u of the stage is considered as constant

$$a_u = u(\bar{c}_{u1} - \bar{c}_{u2}), \quad (1.13)$$

where the u is the circumferential velocity and \bar{c}_{ui} is the averaged circumferential component of the absolute velocity. The subscripts refer to the axial location, 1 being at the inlet and 2 at the outlet of the rotor row.

The $u = r\omega$ is affected only by the radius r and in the case of a linear cascade it is constant, while the rotational speed ω is also constant. \bar{c}_{u2} is not assumed to be influenced by the stator blade geometry so it can be also treated as constant. Thus, \bar{c}_{u1} has to be constant as well. With the area averaging it may be expressed

$$\bar{c}_{u1} = \frac{1}{A_1} \int_{A_1} c_{u1} dA \quad (1.14)$$

where A_1 is the flow area. c_{u1} can be expressed by the means of the axial velocity component c_{x1} and the flow angle α_1 :

$$c_{u0} = \frac{\bar{c}_{x1}}{\tan(\alpha_1)}. \quad (1.15)$$

The flow angle α_1 can be solved with the sine rule

$$\alpha_0 = \arcsin\left(\frac{a}{s}\right) \quad (1.16)$$

Assuming a constant c_{x1} the integral (1.14) can be written as

$$I = \int_M^W \frac{\sqrt{1 - \left(\frac{a}{s}\right)^2}}{\frac{a}{s}} d\left(\frac{z}{h}\right), \quad (1.17)$$

where s is the spacing and a the throat opening illustrated in fig. 1.6.

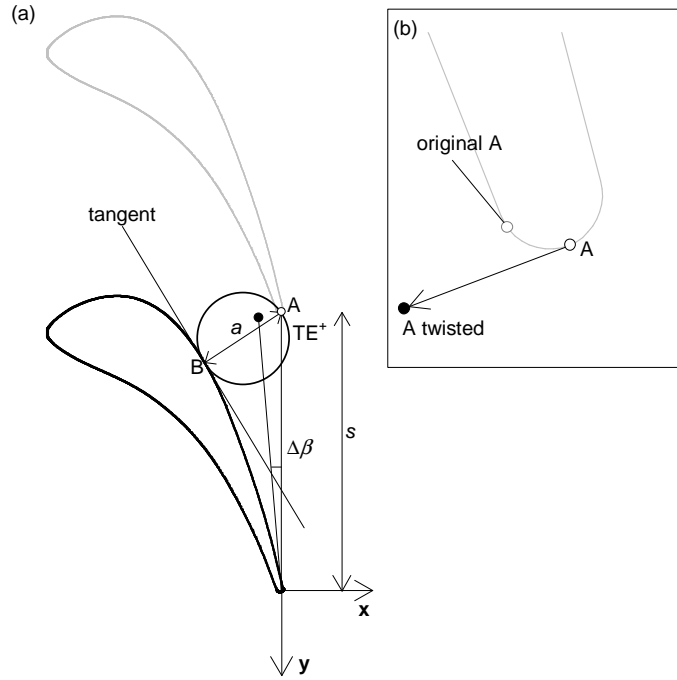


Fig. 1.6: (a) Abbreviations used in calculation of throat opening a (b) Shift of the point A

For a linear cascade the spacing remains constant. The throat opening is often determined graphically, but now as it varies spanwisely a different method is used. In order to find a correlation between the throat opening and the change of the stagger angle, a tangent is laid through point B on the suction side. The general equation for a tangent is

$$ax + by + c = 0 \quad (1.18)$$

where a , b and c are constants. Without causing significant errors, the point A on the trailing edge can be shifted to the spanwisely stacked trailing edge. The variations in the stagger angle $\Delta\beta$ causes the point B to move. In order to simplify the calculation it is useful to consider the point B to be static and correlate the changes in the coordinates of A :

$$\begin{pmatrix} x \\ y \end{pmatrix}_{TE^+} = s \begin{pmatrix} -\sin \Delta\beta \\ \cos \Delta\beta \end{pmatrix}, \quad (1.19)$$

where TE^+ is the trailing edge of the adjacent blade. Thus, the throat opening can be expressed as a distance of the point A , to the tangent:

$$a = \frac{ax + by + c}{\sqrt{a^2 + b^2}}. \quad (1.20)$$

With the equation 1.20 the integral 1.17 can be solved. For a constant specific work a_u and a chosen $\Delta\beta_M$, the change of the stagger angle $\Delta\beta_W$ is obtained.

The geometry was optimized in the work of Schiebenes (2001). It was found that the optimum change of the stagger angle at midspan $\Delta\beta_M$ is -1° .

According to Wingelhofer (2003) there exists also a fair linear relation between the change of the stagger angle at the midspan and at the endwalls:

$$\Delta\beta_W = -2\Delta\beta_M. \quad (1.21)$$

This includes the parabolic form of the change of the stagger angle in the spanwise direction and it is accurate for linear cascades with small $\Delta\beta_M$ (Wingelhofer, 2003).

Chapter 2

Modelling

The physical and numerical models which were used to carry out the simulations are briefly described in this chapter. An example of the command file used to run the simulation in CFX-4.3 is included in the appendix A.

2.1 Off-Design

At the off-design conditions, the turbine is working outside of its nominal, or design point. There the velocity of the working fluid entering the turbine is either reduced or increased. This causes significant change in the inlet flow angle of the second stator row behind the first rotor blades. This can be expressed conveniently with the velocity vectors. The flow leaving from the rotor row and entering the nozzle (stator row) is illustrated in figure 2.1.

The outlet flow angle from the rotor row β_0 is defined as:

$$\beta_0 = \arcsin \frac{a_r}{s_r} + \Delta\beta_0 \left(\frac{a_r}{s_r}, Ma_0 \right). \quad (2.1)$$

Where a_r is throat opening of the rotor cascade, s is spacing for the rotor cascade and Ma_0 is the Mach number at the outlet of the rotor row. The latter term in the equation 2.1 can be neglected if the outlet angle β_0 is about 20° (Müller and Willinger, 2001). Thus, equation 2.1 becomes:

$$\beta_0 = \arcsin \frac{a_r}{s_r}. \quad (2.2)$$

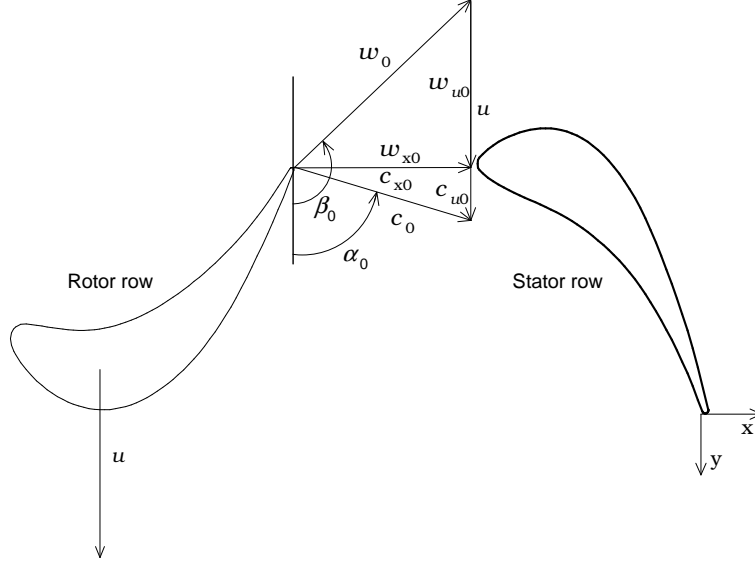


Fig. 2.1: Velocity vectors between the rotor and the stator row.

Which is also known as the "sine rule". Therefore, the rotor outlet flow angle β_0 is affected only by the geometry of the rotor row and can be assumed constant.

Inlet flow to the stator row is defined in the static frame of reference. Thus, the inlet flow vector \vec{c}_0 can be defined as:

$$\vec{c}_0 = \vec{w}_0 + \vec{u}. \quad (2.3)$$

Where \vec{u} is the circumferential speed, defined as:

$$\vec{u} = \omega \cdot r. \quad (2.4)$$

Where ω is angular speed and r is radius. In a linear cascade both are constant, thus:

$$\vec{u} = \text{constant}. \quad (2.5)$$

Therefore the inlet flow to the stator row varies only with the rotor outlet velocity w_0 . The circumferential component c_{u0} of the inlet velocity can be expressed as:

$$\frac{c_{u0}}{c_{x0}} = \frac{w_{u0}}{c_{x0}} + \frac{u}{c_{x0}}. \quad (2.6)$$

Where,

$$\frac{c_{u0}}{c_{x0}} = \frac{1}{\tan \alpha_0} = \cot \alpha_0, \quad (2.7)$$

$$\frac{w_{u0}}{c_{x0}} = \frac{1}{\tan(\beta_0 - 90^\circ)} = \cot(\beta_0 - 90^\circ), \quad (2.8)$$

$$\frac{u}{c_{x0}} = \frac{1}{\phi_0}. \quad (2.9)$$

Where ϕ_0 is flow coefficient. Thus, equation 2.6 becomes:

$$\cot \alpha_0 = \cot(\beta_0 - 90^\circ) + \frac{1}{\phi_0}. \quad (2.10)$$

With equations 2.7, 2.9 and 2.10 the inlet velocity components may be expressed as:

$$c_{u0} = u \phi_0 \cot \alpha_0, \quad (2.11)$$

$$c_{x0} = u \phi_0. \quad (2.12)$$

Throughout rest of the work, the flow coefficient ϕ refers to the stator inlet flow conditions, unless defined and noted explicitly.

Four additional cases were investigated besides the design point. These were 75, 85, 115, 125 percent of the flow coefficient at the design point. The changes in the inlet angle to nozzle row, and the components of the velocity vectors are shown in table 2.1.

Table 2.1: *Inflow parameters for different off-design cases.*

percent	ϕ	α_0	c_{x0}	c_{u0}	c_0
75	0.388	62.8	38.91	25.10	46.30
85	0.439	58.9	44.10	15.06	46.60
100	0.517	90.0	51.88	0.00	51.88
115	0.594	104.2	59.66	-15.06	61.53
125	0.646	111.2	64.85	-25.10	69.53

2.2 Governing equations of the fluid flow

The computational fluid dynamics (CFD) software uses a set of equations to model the fluid flow. The equations are often noted as the *Navier-Stokes* equations. Due to the available computational resources, some simplifications are considered in the modelling. These simplifications are:

- Steady-state calculation.
- Gravitational forces are neglected.
- Turbulence is modelled with an k- ϵ turbulence model.

The simplified *Navier-Stokes* equations comprise the equations for conservation of mass, momentum and energy, and these are: the *continuity equation*:

$$\nabla \cdot \rho \vec{c} = 0 \quad (2.13)$$

the *momentum equation*:

$$\nabla \cdot \rho \vec{c} \vec{c} + \nabla \cdot p = \nabla \cdot \tau_{ij} \quad (2.14)$$

and the *energy equation*:

$$\nabla \cdot \rho \vec{c} \left(e + \frac{\vec{c}^2}{2} + \frac{p}{\rho} \right) = \nabla \cdot (\lambda \nabla T) + \nabla \cdot (\vec{c} \cdot \tau_{ij}) \quad (2.15)$$

Here ρ is the fluid density, $\vec{c} = u\vec{i} + v\vec{j} + w\vec{k}$ the fluid velocity, p the pressure, τ_{ij} is the shear stress tensor and T the temperature. Further μ is the molecular viscosity, and λ is the thermal conductivity.

For solving the 6 unknowns (u, v, w, p, T, ρ) from the equations above, two additional algebraic equations from the thermodynamics is needed. First the *equation of state*, to relate the density to the temperature and to the pressure

$$\rho = \frac{p M}{R T} \quad (2.16)$$

where M is the molecular weight of the fluid, and R is the universal gas constant. Second is the *constitutive equation*, and since the fluid is assumed thermodynamically perfect, the static enthalpy h is only a function of temperature

$$h = c_p T + h_{ref} \quad (2.17)$$

where c_p is the specific heat, assumed to be constant and h_{ref} is the reference enthalpy.

2.3 Fully compressible flow

As the Mach number of the flow velocities exceed 0.2, which is a common boundary for incompressibility, the flow should be treated as fully compressible. With the CFX-4, the full compressibility of the flow requires a high speed version of the SIMPLE pressure coupling method and the Rhie-Chow interpolation method. CFX-4 also encourages the use of "harmonic averaging of the coefficients" switch (CFX-4 Solver Manual ,1997). Fully compressible flow also sets requirements for the inlet- and outlet flow, which is discussed later in the chapter.

2.4 Turbulence

Most turbomachinery flows are turbulent, with laminar regions occurring near the leading edge of the blades. Turbulence influences the aerodynamic and thermodynamic performance of the turbomachines, and therefore its consideration is critical in turbomachinery analysis.

Turbulence is a very complex phenomenon. It is characterized by irregular and random fluctuations in three dimensions. Turbulence is diffusive and dissipative, giving a rise to rapid mixing and increases rates of momentum, heat and mass transfer. Dissipation increases the internal energy of the fluid with velocity fluctuations, at the expense of the kinetic energy in the mean flow.

There exists several books and reviews on the subject of turbulent flow. A good introduction is provided by Schlichting (1979) and White (1991). In this section only the parameters needed for the modelling are briefly described.

2.4.1 Variables defining the turbulence

The basic assumption in the statistical representation of turbulence is that the influence of turbulence on average properties of the flow are of interest, and thus a time average for each of the instantaneous flow equations is considered. Therefore the instantaneous velocity $c_i(t)$ can be defined as:

$$c_i(t) = \bar{c}_i + c'_i, \quad (2.18)$$

where the \bar{c}_i is the mean value and the c'_i represents the fluctuating component, subscript i refers to the components in a cartesian coordinate system ($i = x, y, z$). The same assumption can be done for the other variables:

Temperature T :

$$T_i(t) = \bar{T}_i + T'_i \quad (2.19)$$

pressure p :

$$p_i(t) = \bar{p}_i + p'_i \quad (2.20)$$

and density ρ :

$$\rho_i(t) = \bar{\rho}_i + \rho'_i \quad (2.21)$$

In order to describe the turbulence, is necessary to define the variables that are used. These are:

The *turbulence kinetic energy* k :

$$k = \frac{3}{2} c'^2_i \quad (2.22)$$

And the *turbulence energy dissipation rate* ϵ

$$\epsilon = \frac{C_\mu \cdot k^{1.5}}{l_t}, \quad (2.23)$$

where C_μ is a constant and l_t is the dissipation length scale. ϵ represents the rate which the viscous stresses dissipate the turbulent kinetic energy.

2.4.2 Turbulence model

In this work the Renormalization Group (RNG) $k - \epsilon$ turbulence model is used. Some benefits of the model compared to the standard models (Fluent Inc. 1993):

- Flows in curved geometries are accurately predicted
- The RNG $k - \epsilon$ model is effective in both low and high Reynolds number flow regions. It accounts for the effects of walls and interfaces without empirical data.
- The constants and forms in the RNG $k - \epsilon$ model do not have to be tuned for different problems. No adjustment of parameters is required
- Convergence behavior is robust and the model requires minimal extra computational effort to standard $k - \epsilon$ model

The RNG $k - \epsilon$ model is an alternative to the standard $k - \epsilon$ model for high Reynolds number flows. The model, which derives from a renormalization group analysis of the Navier-Stokes equations (2.13)-(2.15), differs from the standard model only through a modification to the equation for ϵ , except for using a different set of model constants. In the manual of the CFX 4.2 the model was described with following equations:

$$\nabla (\rho \vec{c} k) - \nabla \left(\left(\mu + \frac{\mu_T}{\sigma_k} \right) \nabla k \right) = P - \rho \epsilon \quad (2.24)$$

$$\nabla (\rho \vec{c} \epsilon) - \nabla \left(\left(\mu + \frac{\mu_T}{\sigma_\epsilon} \right) \nabla \epsilon \right) = (C_1 - C_{1RNG}) \frac{\epsilon}{k} (P) - C_2 \rho \frac{\epsilon^2}{k} \quad (2.25)$$

Where μ is the molecular laminar viscosity, μ_T is turbulent dynamic viscosity, P is the production rate and $\sigma_k, \sigma_\epsilon, C_1, C_2$ are constants, described in table 2.2. C_{1RNG} is defined as

$$C_{1RNG} = \frac{\eta \left(1 - \frac{\eta}{\eta_0}\right)}{1 + \beta \eta^3} \quad (2.26)$$

$$\eta = \left(\frac{P_s}{\mu_T}\right)^{1/2} \frac{k}{\epsilon}, \quad (2.27)$$

where η_0 and β are constants (see table 2.2) and P_s is the shear part of the production

$$P_s = \mu_{eff} \nabla \vec{c} (\vec{c} + (\vec{c})^2) \quad (2.28)$$

μ_T is the turbulent dynamic viscosity is defined

$$\mu_T = C_\mu \rho \frac{k^2}{\epsilon}, \quad (2.29)$$

where C_μ is a constant (Table 2.2)). The production rate P is defined as

$$P = P_s - \frac{2}{3} \nabla \vec{c} (\mu_{eff} \vec{c} + \rho k). \quad (2.30)$$

The parameters used in the RNG $k - \epsilon$ model are collected in table (2.2).

Table 2.2: *Constants for the RNG $k - \epsilon$ model.*

C_μ	σ_k	σ_ϵ	C_1	C_2	η_0	β
0.085	0.7179	0.7179	1.42	1.68	4.38	0.015

2.4.3 Fluid properties

The fluid passing through the cascade is air and modelled as ideal gas with constant specific heat capacities (c_p, c_v). A summary of the fluid properties for air with temperature of 20° C and pressure of 1 bar is collected into table 2.3.

Table 2.3: *Fluid properties, (* from (Dubbel, 1990)).*

molecular viscosity *	μ	1.526E-5	kg/ms
molecular weight *	M	28.79	kg/kmol
thermal conductivity *	λ	2.603E-2	J/msK
specific heat capacity *	c_p	1007.0	J/kgK
universal gas constant *	R	8314.0	J/kmolK
reference pressure	p_{ref}	101.3E3	Pa
enthalpy reference temperature	T_{ref}	273.15	K

2.5 Boundary conditions

2.5.1 Inlet

In order to specify the turbulent quantities across the inlet, a common way is expressing the values of k and ϵ as mean flow characteristics. This is done by specifying a turbulence intensity I and a dissipation length scale l_t .

Turbulence intensity I describes the ratio of the average velocity fluctuations in respect to the main flow velocity and is defined as

$$I = \frac{\sqrt{\frac{2}{3}k}}{c}, \quad (2.31)$$

where k is the turbulence kinetic energy defined in the equation 2.22. In this work I is chosen according to the ERCOFTAC test-case to $I = 0.02$.

The dissipation length scale l_t can be estimated in turbomachinery as one per mille of the spacing s

$$l_t = 0.001 \cdot s = 4.78 \cdot 10^{-5} \text{ m}. \quad (2.32)$$

The value is based on experience and it affects mainly on the mobility of the vortices.

To specify the flow velocity at the inlet, the 1/7 power law is applied to model the boundary layer effect on the velocity profile. Boundary layer thickness δ

is chosen according to the ERCOFTAC test-case to 9 percent of the blade height:

$$\frac{\text{b. l. thickness}}{\text{blade height}} = \frac{\delta}{h} = 9\% \quad (2.33)$$

$$h = 55\text{mm} \rightarrow \delta = 4.95\text{mm} \quad (2.34)$$

Then the power law can be applied.

$$u_0 = \begin{cases} u_0 & z < h - \delta \\ u_0 \cdot \left(\frac{z}{\delta}\right)^k & z \geq h - \delta, \quad k = 1/7 \end{cases} \quad (2.35)$$

The inlet velocity in the axial direction $u_{1ax} = 51.878\text{m/s}$, is from the ERCOFTAC test-case. The velocity distribution at the inlet is illustrated in figure 2.2

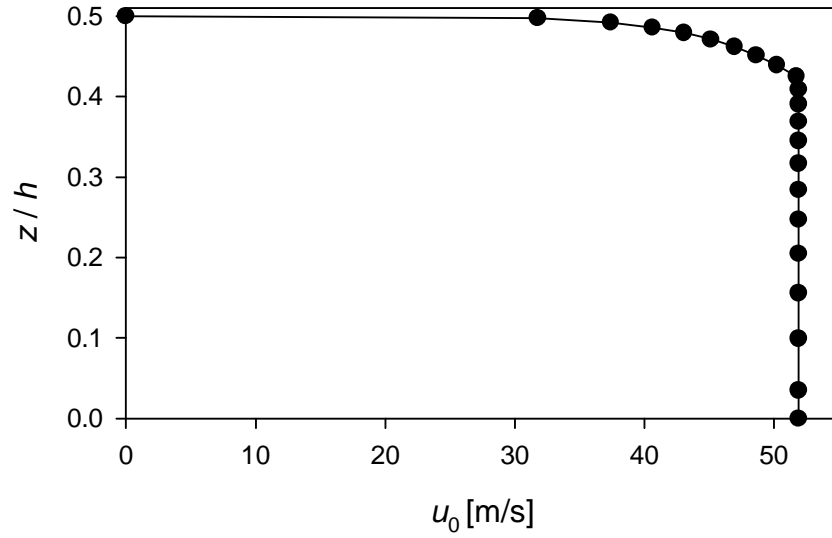


Fig. 2.2: *Velocity distribution at the inlet*

Static temperature at the inlet $T_0 = 304.41$ K is chosen from the ERCOFTAC test-case.

2.5.2 Walls

Boundary conditions for the turbulence equations are specified using wall functions. In the light of the experimental evidence it is reasonable to expect the *logarithmic wall profile* for the velocity, in the vicinity of the walls. The *No-slip* condition is invoked to provide zero tangential velocity for the fluid at the walls. There is neither heat flux across the walls.

2.5.3 Outlet

At the outlet, a pressure boundary is set, and the Neumann boundary conditions are applied to all transported variables, velocity, k , ϵ , temperature etc. This means that their gradients are specified, rather than their values. All transported quantities are given zero normal gradient.

For the pressure boundary static pressure is set to:

$$p_1 = 4.518 \cdot 10^4 \text{ Pa} \quad (2.36)$$

While the reference pressure is set to $p_{ref} = 101300 \text{ Pa}$.

2.5.4 Symmetry

The symmetry plane is set to $z = 0$, it equals midspan in the cascade. The boundary conditions at the symmetry plane are quite straightforward. All variables are mathematically symmetric, with no diffusion across the boundary, except the component of velocity normal to the boundary and the component of the Reynolds shear stress and Reynolds Flux involving the normal velocity, which are anti-symmetric.

2.5.5 Periodicity

Periodicity is a mathematically simple boundary condition. It ensures that all variables, and hence also all coefficients, have the same value at both ends of the computational or physical domain. With the periodicity, it is possible

to repeat the geometry to infinity in specified direction. Here it is applied to produce a linear cascade by creating the mesh only for one nozzle and then repeating it in circumferential (y) direction.

2.6 Mesh

There are two types of mesh models. They differ by the data structure used to describe the mesh itself. A *structured mesh* consists of a set of points and regular connections at each point such that these connections can be stored as matrix.

The unstructured meshes cannot be described within the same way of the structured models. Additional information is needed to specify the mesh. Since the connections of each point are not regular connections, they should be explicitly defined and stored. The unstructured meshes does not keep the global information of the whole mesh, thus they are more appropriate to define complex geometric domains.

The mesh was created with CFX-4.3 Meshbuild. Mesh is structured, since it has an advantage of being faster for the solver, compared to the unstructured mesh. This is due to the fact that an implicit relationship between the number of a cell and the number of its neighbors exists. In figure 2.3, z-plane of the mesh is illustrated at the midspan.

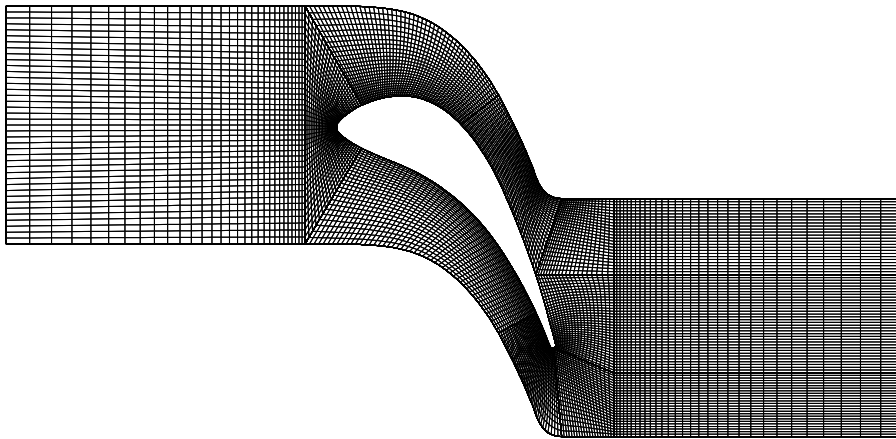


Fig. 2.3: *The mesh in the z-plane at the midspan*

The nozzles were cut in half in spanwise direction at the midspan, exploiting

the symmetry. This was possible with the simplification from a annular to a linear cascade. With the use of periodicity the cascade was modelled with one blade and flow channel. In order to reduce the effect of the inlet/outlet regions, the inlet was set to 1.25 times the chord length upstream of the leading edge. Respectively, the pressure boundary at the outlet was set 1.25 of the chord length downstream of the trailing edge. This for minimizing the effect of the pressure boundary on the flow right after the nozzles.

The mesh is divided into 12 blocks. Figure 2.4 illustrates how the blocks are organized. Mesh contains in total 214 000 cells. How cells are divided in each blocks is represented in table 2.4.

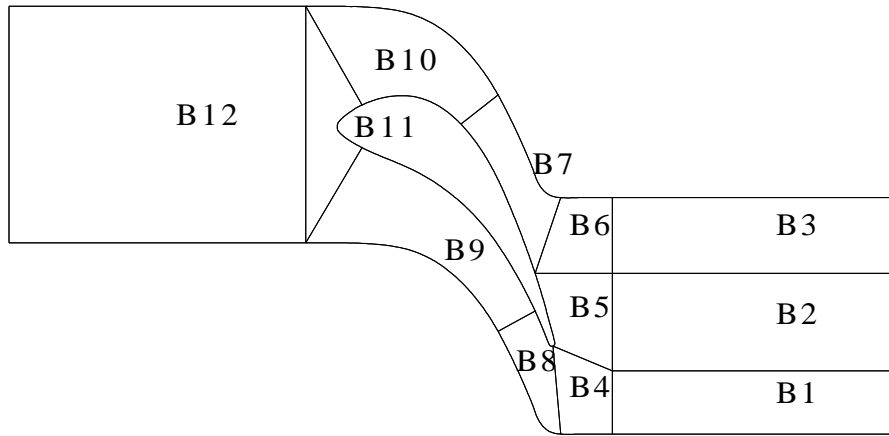


Fig. 2.4: *Numbering and division of the blocks*

The boundary layer modelling introduces always problems. With a inviscid flow the problem rises with turbulent boundary layers. The grid should be densified highly in the vicinity of the walls. That is one of the main points why the wall functions are commonly used. With the wall functions, number of cells in a mesh can be even half of what would be required without them (Siikonen, 2001). The wall function applies only for the flat plate boundary layer, when the pressure gradient is zero. With high Reynolds number turbulence model, combined with the wall function, a special consideration has to be directed to the cell size close to the wall. A common measure for the acceptable cell size is y^+ , which is defined as:

$$y^+ = \frac{\rho u_\tau y}{\mu} \quad (2.37)$$

Table 2.4: *Cell distribution in blocks.*

BLOCK	NI	NJ	NK	NCELL
1	25	30	20	15000
2	35	30	20	21000
3	25	30	20	15000
4	25	20	20	10000
5	35	20	20	14000
6	25	20	20	10000
7	25	35	20	17500
8	25	35	20	17500
9	25	50	20	25000
10	25	50	20	25000
11	25	40	20	20000
12	40	30	20	24000
TOTAL			=	214000

where u_τ is the friction speed. According to Siikonen (2001) the range of the y^+ should be:

$$30 < y^+ < 300 \quad (2.38)$$

If the value is higher, then the significance of wall function disappears and flow is treated frictionless. Design process of the mesh is always iterative, until the y^+ values are in the acceptable range.

On the geometrical point of view, the most challenging part of meshing is in the vicinity of the trailing edge. The blocks needed to be designed so that the skewness of the cells around the trailing edge would be as small as possible. An enlargement of the final mesh around the trailing edge is illustrated in figure 2.5.

The mesh was created for the Cylindrical nozzles and then modified with an subroutine for the Compound Lean and Controlled flow nozzles. The mesh for the Cylindrical nozzles needed to be designed so that the leaning and twisting of the profile in the modified nozzles would not result in heavily skewed cells.

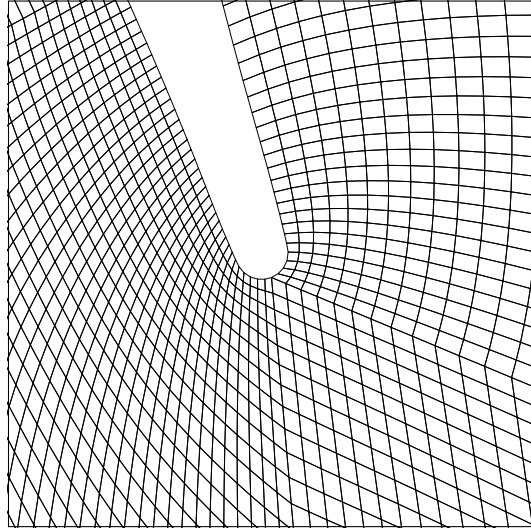


Fig. 2.5: *Mesh around the trailing edge of the Cylindrical nozzles*

2.6.1 Cylindrical nozzles

The mesh for the Cylindrical nozzles was created in CFX-4.3 Meshbuild. The profile coordinates from the ERCOFTAC test-case were imported and the grid was created around the profile in 2-D, and after that extruded to 3-D. The mesh for the Cylindrical nozzles was used then afterwards for the other two nozzles, by modifying it with a subroutine in the CFX-4 Solver. Therefore in the design, was important to consider the upcoming modifications of the mesh. The generated grid is illustrated in figure 2.6.

2.6.2 Compound lean nozzles

Mesh for the Compound lean nozzles was created by modifying the mesh constructed for the Cylindrical nozzles. The modification was done by shifting the cells in circumferential direction in respect to the spanwise distance from the endwall. The principle of the leaning was described in the chapter 1.2.5. The modification was applied in a subroutine inside the Solver. The resulted grid is illustrated in figure 2.6.

2.6.3 Controlled flow nozzles

The mesh for the Controlled flow nozzles was created in a similar manner to Compound lean nozzles, with an subroutine in the CFX-4 Solver. The twisting of the mesh was done by shifting the cell nodes in appropriate manner so that the profile corresponded to the shape of the designed profile. The method for creating the Controlled flow nozzles is described in the chapter 1.2.6. The modified grid is illustrated in figure 2.6.

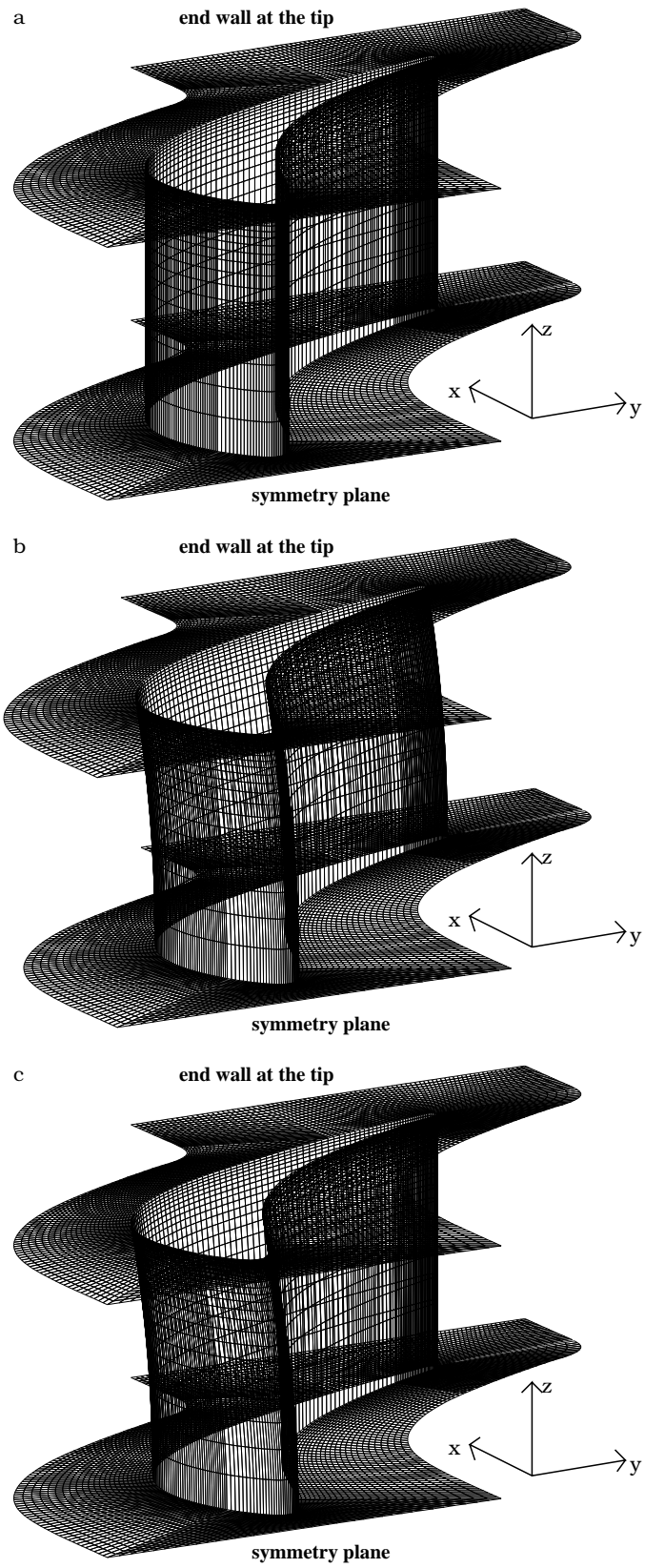


Fig. 2.6: Grid of the a: Cylindrical nozzles, b: Compound lean nozzles and c: Controlled flow nozzles.

2.7 Solver

2.7.1 Finite Volume method

In order to solve computationally the governing partial differential equations (2.13, 2.14 and 2.15) of the fluid flow, they have to be transformed into equations that contain only numbers, while the combination of these numbers is described by the simple operations.

Producing the transformation of a partial differential equation to what is known as a numerical analogue of the equation, is called *numerical discretisation*. In this discretisation process, each term within a partial differential equation must be translated into a numerical analogue, that the computer can be programmed to calculate.

The finite volume method is a numerical method for solving partial differential equations that calculates the values of the conserved variables averaged across the volume. The finite volume method is preferable to other methods as a result of the fact that boundary conditions can be applied noninvasively. This is true because the values of the conserved variables are located within the volume element, and not at nodes or surfaces.

The physical space is split up into small volumes and the partial differential equations are integrated over each of these volumes in *the finite volume method*. Then, the variables are approximated by their average values in each volume and the changes through the surfaces of each volume are approximated as a function of the variables in neighboring volumes.

The basis of the code CFX-4 uses is a conservative finite difference, or finite volume method with all variables defined at the center of control volumes which fill the physical domain being considered. Each equation is integrated over each control volume to obtain a discrete which connects the variable at the center of the control volume with its neighbors. All terms in all equations are discretised in space, using second order centered differencing scheme, apart from advection terms and the convection coefficients obtained by the improved Rhie-Chow interpolation formula. The treatment of the advection terms determines the accuracy of the solutions of the model equations in CFX-4. The choice of the discretisation methods available varied from simple

diffusive UPWIND schemes to bounded quadratic upwind schemes. With the possible cost in accuracy the choice was a HYBRID differencing scheme. In the HYBRID differencing scheme, the CENTRAL differencing is used if the mesh Peclet number is less than 2, and UPWIND differencing is used if the Peclet number is greater than 2, but then ignoring diffusion. More details of the schemes can be found from the literature and CFX-4 Solver manual.

2.7.2 Data export

The data is extracted and interpolated in 4 different planes through the model. Locations of the planes are shown in figure 2.7, where is also illustrated the dimensional and non-dimensional axes, which are used in the following chapters.

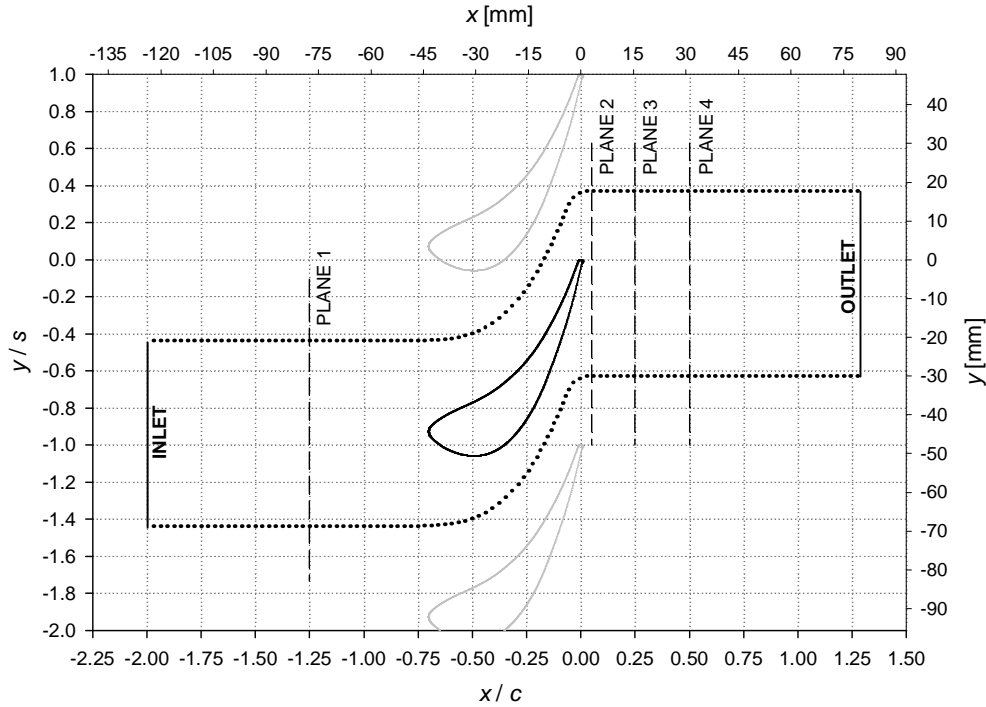


Fig. 2.7: *Locations of the planes in two coordinate systems.*

The first plane from downstream of the inlet is located so that the effect of the inlet boundaries and the blade is minimized. The second plane is right after the cascade 5 percent of the chord length behind the trailing edge. Third plane is 15.5 millimeters downstream from the trailing edge, which corresponds to 25 percent of the chord length, it is also in the vicinity of

the rotor cascade of the ERCOFTAC test-case. The last plane is located 50 percent of the chord length downstream of the trailing edge.

2.7.3 Post-processing

The three-dimensional numerical simulation provides enormous amounts of data for post-processing, even in steady-state calculation. In order to reduce the data extracted from the planes, an averaging procedure by Kreitmeier is applied. It computes averaged values with losing least amount of information as possible, using balance equations of fluid mechanics and thermodynamics, in order to guarantee the consistency of the flow parameters illustrated by averaged values. The procedure reduces gradually the generally four-dimensional data (fourth dimension is the time) on three, two dimensional or linear representation (Kreitmeier, 1977).

Chapter 3

Secondary flow and losses

3.1 Secondary flow

When the flow is turned by a blade row in an axial turbomachine, the flow far away from the endwall can often be considered as two-dimensional. The boundary layer flow along the endwalls contains spanwise velocity gradients. When the boundary layer flow is turned, transverse velocity components are introduced. The two dimensional flow is termed *primary flow* and the three-dimensional effect near the endwalls is called *secondary flow*. The secondary flow is supposed to be a small disturbance superimposed on the primary flow. In practise, the secondary flow can be very large.

3.1.1 Secondary flow and vorticity

The pressure gradient working from the pressure side to the suction side, introduces a crossflow near the endwall from the pressure side to the suction side. The flow in the boundary layer has a lower velocity than the flow further away from the endwall. Since the pressure gradient, working on the fluid, is determined by the flow outside the boundary layer, the boundary layer flow has a smaller radius in turning than the outside flow. The counter action of the endwall crossflow appears further away from the endwall and results in vortices. An example of the flow through a blade passage is illustrated in figure 3.1.

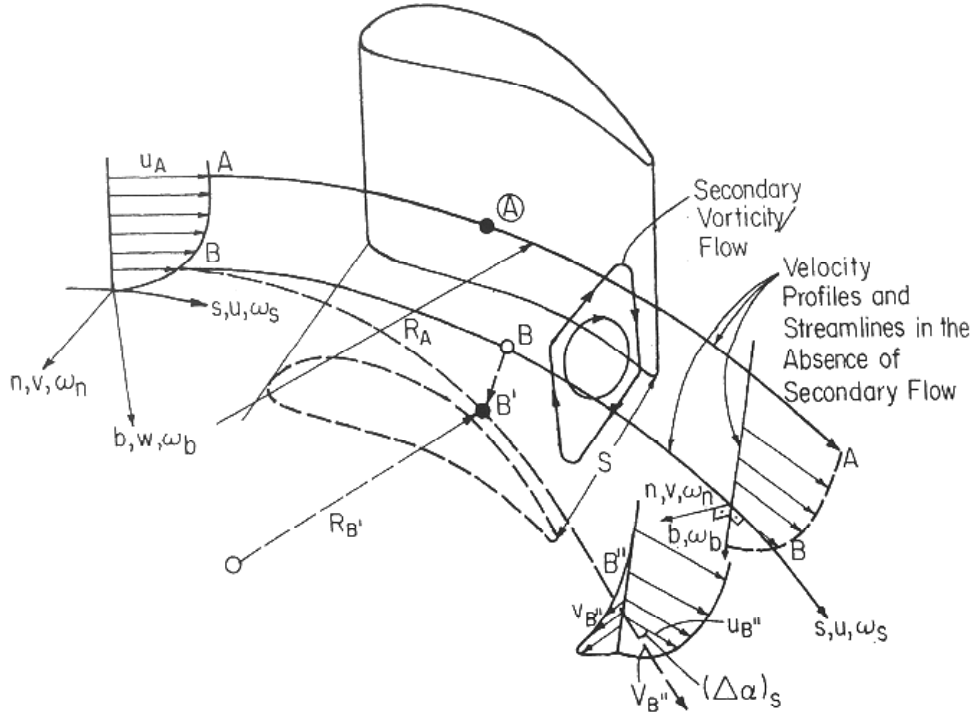


Fig. 3.1: *Flow through a cascade (Lakshminarayana, 1997).*

One of the most comprehensive studies of the secondary flow has been done by Sieverding (1985) where the previous research done in this field is gathered. The most recent review is from Langston (2001).

Sieverding (1985) classified the flow phenomena which occur in a passage:

- Horseshoe vortex, with a pressure side leg and suction side leg.
- Passage vortex.
- Counter vortex at the suction side, also called corner vortex.
- Trailing edge vortices.

These vortices are listed in order of their appearance as the fluid flows through the cascade. Their interaction is the main reason for the difficulties in the prediction and modelling of their affect in the loss generation.

Development of the vortices

The horseshoe vortex is developed when the flow meets the leading edge of the blade. The high energy fluid in the edge of the boundary layer partly

passes the leading edges in axial plane, but also flows towards the endwall, turning back to upstream close to the wall. As the flow continues its way around the leading edge it turns into a vortex. The blade camber sets also non-symmetry between the pressure- and suction side legs of the horseshoe vortex. The strength of the horseshoe vortex depends mainly of the leading edge radius.

The suction side leg of the horseshoe vortex remains close to the blade and travels downstream in the corner of the endwall. It diffuses and dissipates before it reaches the trailing edge.

The pressure side leg detaches from the blade and crosses the passage, merging with the passage vortex near the suction side of the blade.

The passage vortex dominates the vorticity in the latter part of the passage. The development of the passage vortex is combination of the pressure side leg of the horseshoe vortex and the crossflow near the endwall. As the passage vortex is the biggest of the vortices developing in the channel, it also causes most of the losses. Gregory-Smith and Graves (1983) showed that the loss core does not coincide with the passage vortex center, even though it follows the movement.

The blade trailing edge creates additional vorticity, called trailing edge vortices. These are in the direction of the flow, and they are developed from the pressure gradient over the trailing edge. In the vicinity of the trailing edge it is possible to find several vortices which quickly merge into one big vortex. The overall vorticity is dominated by the passage vortex.

3.1.2 Influences of the secondary flow

The secondary flow has many consequences in axial turbomachines. Gregory-Smith (1997) and Lashminarayana (1996) have summarized them:

- Secondary flow introduces cross-flow velocity components, which result in three-dimensionality in the flow field.
- The secondary flow tends to form a vortex, which will eventually initiate a separation region near the suction surface of the wall. Their effect on the overall performance is thus substantial.

- Vorticity causes changes in the outlet flow angle, which may result changes in the work output.
- The secondary flow introduces incidence changes in the downstream row. The rotor-stator interaction, due to secondary flow, results in unsteady flow/pressure field in subsequent blade rows. This interaction may result in vibration, flutter and noise.
- The secondary flow has appreciable effect on the flow turning (usually overturning in the wall regions and underturning outside the wall region), thus affecting the pressure drop in turbines.
- Secondary flow may increase the heat transfer and decrease the effect of cooling.
- The resulting loss decreases efficiency. The endwall flow losses, including secondary flow, accounts for approximately 2-4 % drop in the efficiency of turbomachines.
- Secondary flow affects the temperature field as well as the cooling requirement in the turbine.

Therefore, it is reasonable to note that the secondary flow plays an important role in the design and development of the axial flow turbomachinery. Thus, the influence has to be considered while investigating the aerodynamic behavior of different nozzles.

3.2 Losses

3.2.1 Loss generation

The losses at the exit of a blade row is often determined as the massflow averaged total pressure difference over the blade row, related to the dynamic pressure at the exit.

$$Y_t = \frac{\bar{p}_{t0} - \bar{p}_{t1}}{\bar{p}_{t1} - \bar{p}_1} \quad (3.1)$$

Other definitions, may be in terms of enthalpy changes. In this work losses refer to the loss in total pressure.

3.2.2 Secondary losses

Secondary loss may be defined as the difference between the total loss (ξ_{tot}) and the two-dimensional profile loss of the blade (ξ_p). The latter may be the midspan loss, if the blade aspect ratio is high. Secondary loss determined this way is often termed *gross* secondary loss ($\xi_{sec,gross}$), as it includes the loss at the inlet due to the incoming endwall boundary layers. The *net* secondary loss ($\xi_{sec,net}$) is the total loss minus the profile loss minus the inlet loss (ξ_{inlet}).

$$\xi_{sec,gross} = \xi_{tot} - \xi_p, \quad (3.2)$$

$$\xi_{sec,net} = \xi_{sec,gross} - \xi_{inlet}. \quad (3.3)$$

Since the secondary loss affects the region near the endwalls, the secondary loss is less important for high aspect ratio blades. When the aspect ratio is high enough so that the secondary flow regions do not interact, it has been shown that the secondary loss is inversely proportional to the aspect ratio. (Gregory-Smith, 1997).

Gregory-Smith (1997) also suggested that the secondary loss is a function of the following parameters:

- aspect ratio, since the losses are averaged over the whole span.
- blade loading, since the turning of the flow will affect the strength of secondary flows.
- inlet boundary layer thickness and condition, again affecting secondary flows.
- Reynolds number.
- Mach number.
- blade geometry.

3.2.3 Profile losses

The losses due to blade boundary layers (including separated flow) along the blade surfaces and due to the wake through viscous and turbulent dissipation are classified "profile losses". The mechanical energy is dissipated into heat within the boundary layer. This increases the entropy and results in stagnation pressure loss. In addition, the non-uniform velocity profiles in both of the boundary layer and the wake (bounded and shear flows) are smoothed out by viscous and turbulent effects. The magnitude of the profile loss mainly depends on the velocity, roughness of the blade surfaces, Reynolds number and the blade profile.

In many instance, a separate category called "trailing edge loss" is included to account for losses due to the finite thickness of the blade trailing edge, which causes flow separation and shock-expansion-wave interactions due to sharp corners. This loss could be appreciable in transonic and supersonic turbines. In subsonic turbines this loss is used to be classified and taken account inside the profile losses (Wei, 2002).

Usually the profile loss is evaluated as the midspan loss, where the two-dimensional flow appears. This is valid only for blades with a high aspect ratio, where the flow at midspan is not affected by the endwalls. Simulation the flow through a linear cascade numerically by the means of CFD, a symmetry boundary condition is applied at midspan for a reduction of the computational domain. Since only the normal gradient is set to zero, no flow field is obtained exactly at midspan. The determination of the profile loss is done then as near as possible to midspan. The stagger angle of controlled flow nozzles changes radially. This causes differences to the profile loss, and it cannot be obtained from the midspan or at the point where the change of the stagger angle is 0° . Latter, because at that point the flow is highly 3-dimensional. This is the reason why in this research losses are not separated and only total losses are investigated.

Chapter 4

Results of the CFD

4.1 Secondary velocities

4.1.1 Calculation of the secondary velocity vectors

In order to visualize the secondary flow and the vortices, it is common to use secondary velocity vector. These are velocity vectors in planes perpendicular to the primary flow direction. For visualizing the vortices, in this work plane 3 is chosen (See fig. 2.7). The secondary velocity vectors are calculated as the difference of the velocity from the primary velocity. The primary outlet flow angle, with respect to the pitchwise direction, α_{prim} is set to

$$\alpha_{prim} = 20^\circ. \quad (4.1)$$

This angle was given in the ERCOFTAC test-case as design outlet flow angle. The averaged outlet flow angles, obtained from the simulations, were found to correlate to the primary outlet flow angle. The length of the primary velocity vector c_{prim} is calculated from the averaged velocities at the given point:

$$c_{prim} = \sqrt{c_x^2 + c_y^2}, \quad (4.2)$$

where c_x stands for the axial velocity component and c_y is the circumferential velocity component. Note that the vectors $vecc_{prim}$ and \vec{c} have the same

absolute length but different angle. The abbreviations used in defining the different velocity components are illustrated in figure 4.1.

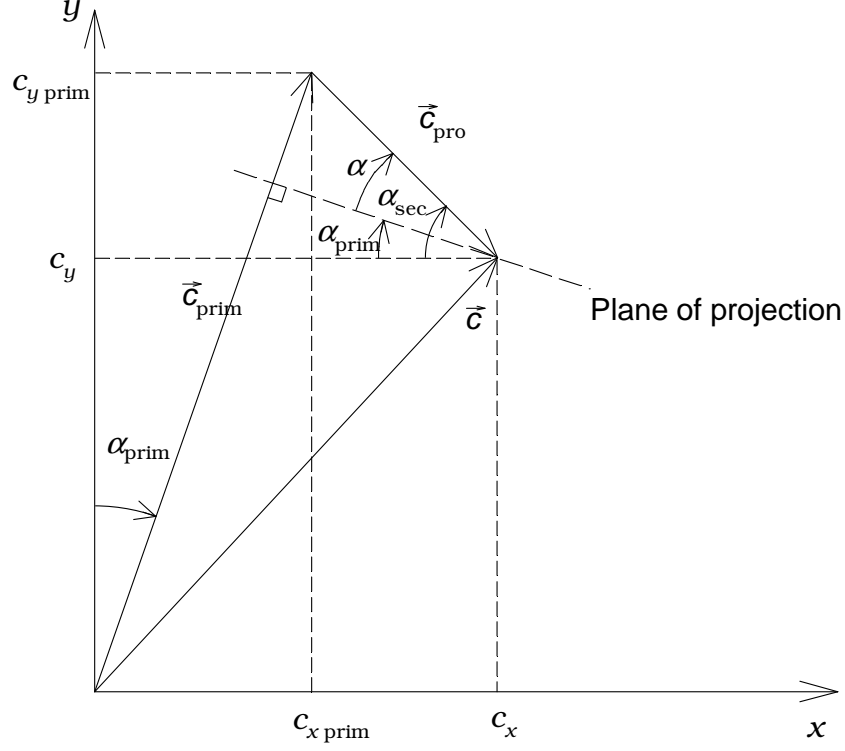


Fig. 4.1: *Secondary and primary velocity vectors.*

The primary velocity c_{prim} can be divided into its components by the means of the primary outlet flow angle α_{prim} . The spanwise component of the velocity c_{zprim} is set to be zero:

$$\begin{pmatrix} c_x \\ c_y \\ c_z \end{pmatrix}_{prim} = c_{prim} \cdot \begin{pmatrix} \sin \alpha_{prim} \\ \cos \alpha_{prim} \\ 0 \end{pmatrix} \quad (4.3)$$

The secondary velocity components can be calculated as follows:

$$c_{xsec} = c_x - c_{xprim}, \quad (4.4)$$

$$c_{ysec} = c_y - c_{yprim}, \quad (4.5)$$

$$c_{zsec} = c_z. \quad (4.6)$$

The angle of the secondary velocity vectors α_{sec} is defined as:

$$\alpha_{sec} = \arctan\left(\frac{c_{ysec}}{c_{xsec}}\right). \quad (4.7)$$

The magnitude of the secondary velocity at the given point is:

$$c_{sec} = \sqrt{c_{xsec}^2 + c_{ysec}^2 + c_{zsec}^2}. \quad (4.8)$$

4.1.2 Secondary velocity vector plots

In order to create the plots by using vectors, two parameters are needed. These are the length and the angle of the vectors. Therefore, it is necessary to calculate the difference between the primary and secondary velocity angle α the circumferential component of the velocity c_{pro}

$$\alpha = \alpha_{sec} - \alpha_{prim} \quad (4.9)$$

$$c_{pro} = |c_{sec}| \cdot \sin(\alpha) \quad (4.10)$$

The plotted secondary velocity vector consists of two components: the span-wise component c_z and the circumferential component c_{pro} . As both are known, the angle δ and the length l of the vectors can be calculated with the help of trigonometry:

$$\delta = \arctan\left(\frac{c_z}{c_{pro}}\right) \quad (4.11)$$

$$l = \sqrt{c_{pro}^2 + c_z^2} \quad (4.12)$$

The created plots are illustrated in figures 4.2 to 4.6. The vector scales are kept constant, in order to help the comparison between the different off-design conditions. The superpositioned location of the trailing edge is marked in figures, with ps referring to the pressure side and ss referring to

the suction side. The trailing edge is located between these, upstream in the flow direction.

The plots of the compound lean nozzles some vectors are missing on the left side. This is due to the leaning of the blade.

4.1.3 Identification of the vortices

In figure 4.4 two vortices can be identified. Close to the endwall and in the circumferential distance of -0.5 the *passage vortex* appears, in plot of the *compound lean nozzles* also the *trailing edge vortices* are visible, which are shown as one big vortex with low magnitude. The passage vortex can be identified by its sense of rotation, since the vectors close to the endwall have the same direction as the endwall cross-flow. Also the location of the vortex, in the vicinity of the endwall, and the size indicates to this particular vortex. The second vortex is located closer to the superpositioned trailing-edge, the sense of rotation is opposite that of the passage vortex and the strength is weaker. This indicates that the vortex is the merged trailing edge vortices. It is hard to say if there really exists only one trailing edge vortex or the separated vortices just appear as one big vortex.

Placement of the vortices

While comparing figure 4.2 to 4.4, the movement of the passage vortex is noticeable. As the flow coefficient rises, the passage vortex moves in the passage in the direction from the pressure side to the suction side. The movement is stronger at part load (figure 4.2 and 4.3) than at over load (figure 4.5 and 4.6). At low over load compared to the design point there is no significant change in the circumferential position of the vortex center (figure 4.4 and 4.5). At high over load (figure 4.6) the passage vortex center moves back to the direction of the pressure side.

In the spanwise direction the center of the passage vortex is moving away from the endwall as the flow coefficient rises. The path of the movement is similar for all investigated nozzles. The movements can be assumed to be a result of two factors: The change in the inlet flow angle, which affects the

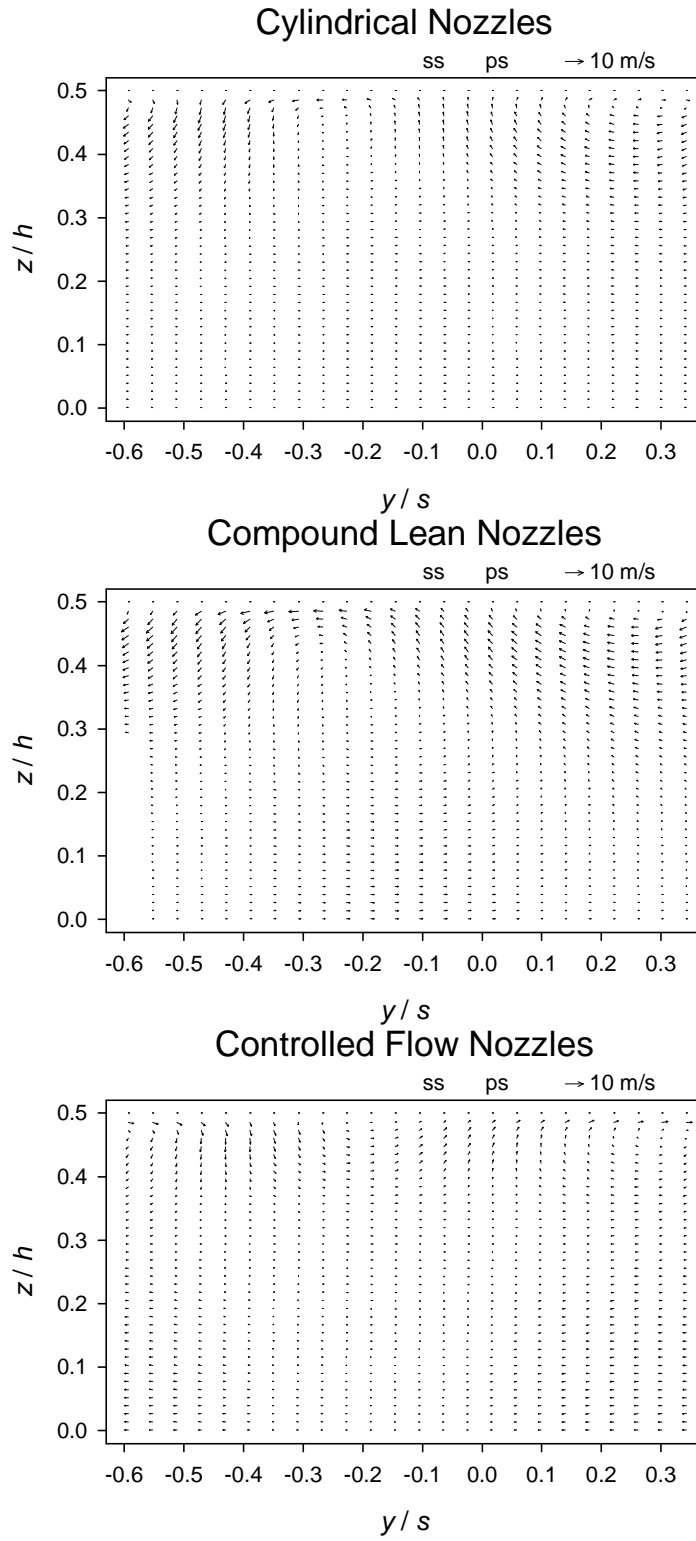


Fig. 4.2: Secondary velocity vectors downstream of the cascade, for $\phi = 0.75 \cdot \phi_{DP}$.

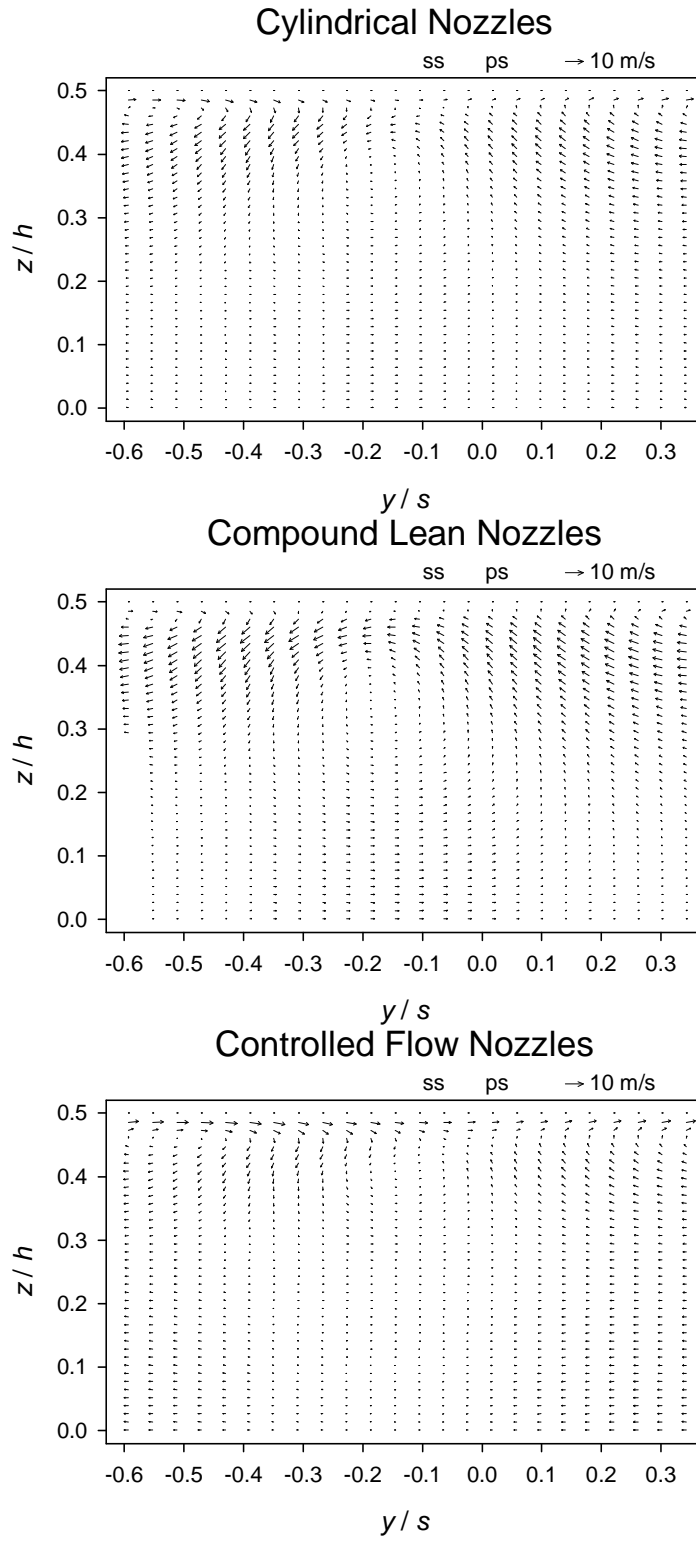


Fig. 4.3: Secondary velocity vectors downstream of the cascade, for $\phi = 0.85 \cdot \phi_{DP}$.

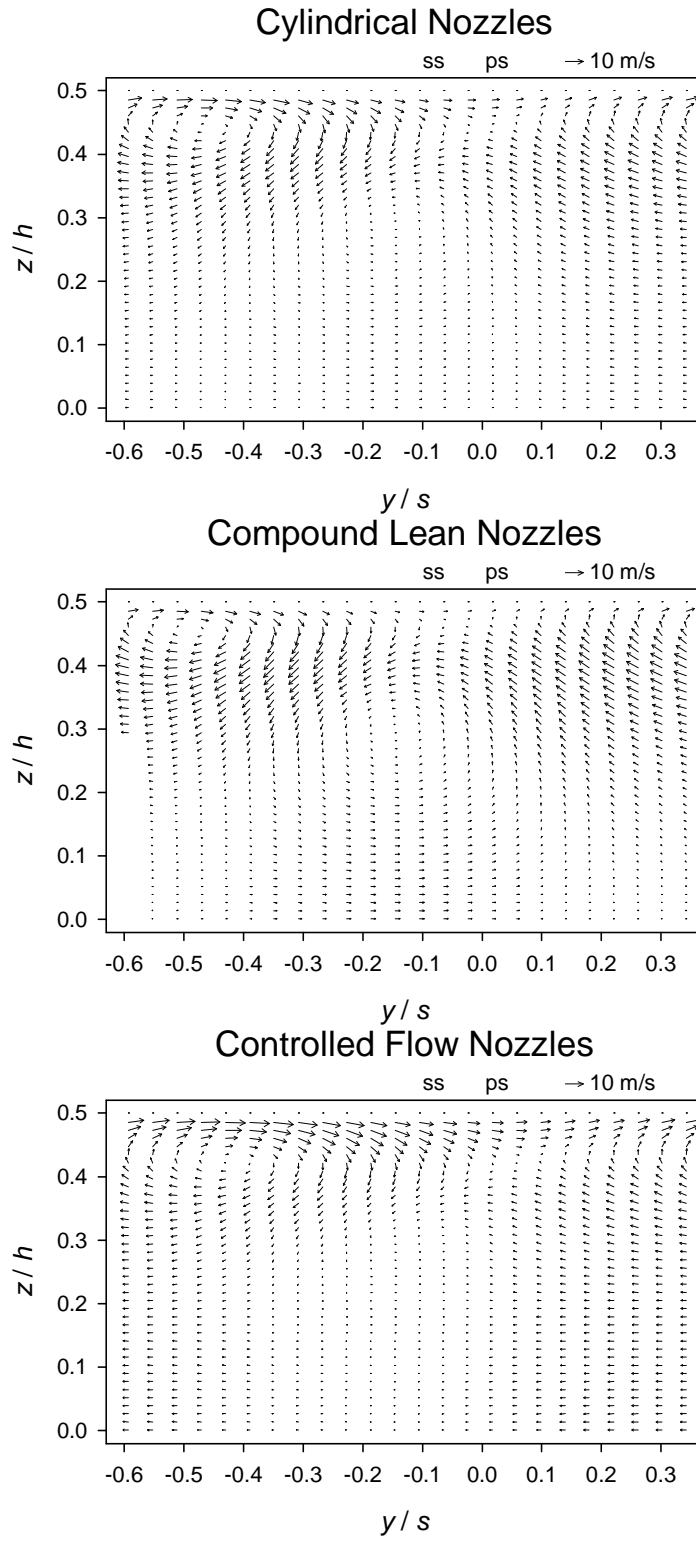


Fig. 4.4: *Secondary velocity vectors downstream of the cascade, for $\phi = 1.00 \cdot \phi_{DP}$.*

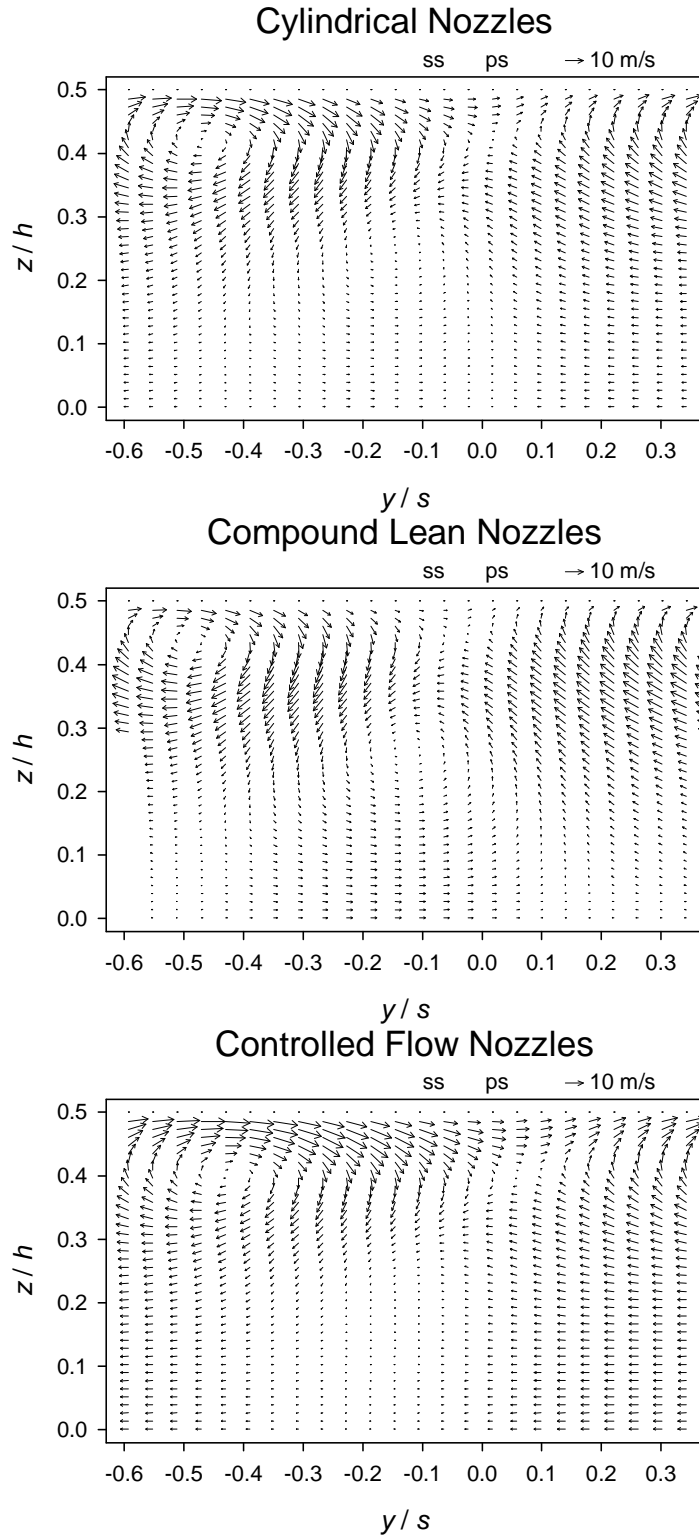


Fig. 4.5: Secondary velocity vectors downstream of the cascade, for $\phi = 1.15 \cdot \phi_{DP}$.

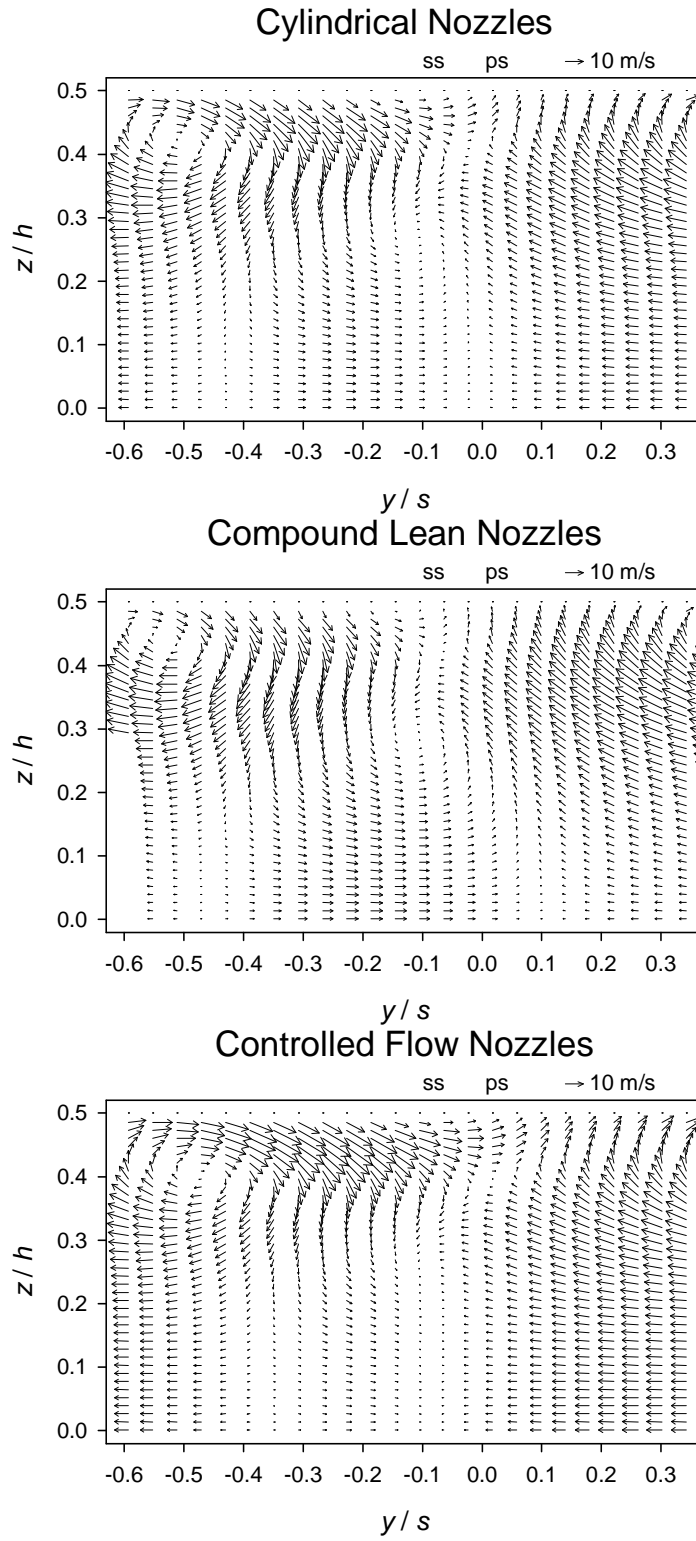


Fig. 4.6: *Secondary velocity vectors downstream of the cascade, for $\phi = 1.25 \cdot \phi_{DP}$.*

circumferential placement of the vortex center, and the increased massflow, strengthening the vortices which pushes the center further away from the endwall.

The movement of the trailing edge vortex center for increasing flow coefficients, is from the pressure side to the suction side. The trailing edge vortex moves also in the spanwise direction. The movement is in the same direction, from the endwall towards the midspan, as that of the passage vortex. While comparing the placement at different flow coefficients, it seems that the growth of the passage vortex affects the radial and as well as the circumferential position of the trailing edge vortex.

4.1.4 Secondary flow at off-design

While comparing figure 4.2 to 4.6, it is noticeable how the secondary velocities increase with the flow coefficient. This is evident as the massflow and velocities increase.

Part load

As the vector scale is kept constant, it is possible to compare the overall secondary velocities at different flow coefficients. Compared to the design point, figure 4.4, the secondary velocities at part load (figure 4.2 to 4.3) decrease in general with the flow coefficient. Downstream of the compound lean nozzles, the secondary velocities are highest in the region $z/h = 0.3 - 0.5$ and also near the midspan, in the wake. The higher secondary velocities appear downstream of the controlled flow nozzles in the center of the passage. The endwall crossflow is also higher downstream of the compound lean nozzles than downstream of the other nozzles.

Over load

At over load, the highest secondary velocities appear on the same sections downstream of the passage as at part load. Downstream of the compound lean nozzles the secondary velocities are highest on the quarter close to the

endwall in the passage. Also the region close to the midspan, in the vicinity of the trailing edge, has higher secondary velocities than other regions. Downstream of the controlled flow nozzles, high secondary velocities appear through out the quarter close to endwall. Near the the trailing edge, on the quarter close to the midspan, secondary velocities are lower compared to the other regions.

The differences can be affected by the change in the stagger angle which was not considered while calculating the secondary velocities. The passage vortex appears to be stronger downstream of the controlled flow nozzles than downstream of the compound lean nozzles. Vice versa, the trailing edge vortices are clearly visible downstream of the compound lean nozzles, downstream of the controlled flow nozzles they do not appear clearly as one big vortex. The trailing edge vortex appears clearly downstream of the cylindrical nozzles and the magnitude of the passage vortex is greater than on the two other nozzles.

4.2 Mass flow density

In order to express the mass flow flowing through the passage, it is more convenient to use the mass flow density than the mass flow itself. This is as the mass flow density Q_m represents the mass flow related to the flow area. Thus, the flow area is not needed for the calculation and the values are independent of the geometry. The mass flow density Q_m is defined as:

$$Q_m = c_x \cdot \rho, \quad (4.13)$$

where c_x is the axial velocity and ρ_i is the density.

The mass flow density varies with different flow coefficients. In table 4.1 are presented the corresponding mass flow density rates downstream of the nozzles for different flow coefficients. In table 4.1, the ratio of flow coefficient is defined at the inlet, not at the outlet like the mass flow density.

The nozzles differ on their method in the distribution of the mass flow. Compared to the *cylindrical nozzles*, the *controlled flow nozzles* reduce the mass

Table 4.1: *Massflow density for different flow coefficients.*

ϕ/ϕ_{DP} [%]	75	85	100	115	125
$Q_{m,CYL}$ $\frac{kg}{m^2s}$	70	82	103	131	166
$Q_{m,CLN}$ $\frac{kg}{m^2s}$	70	82	102	130	164
$Q_{m,CFN}$ $\frac{kg}{m^2s}$	70	82	103	131	167

flow density at the tip and at the hub of the blade and increase it on the midspan region. The *compound lean nozzles* increase the mass flow downstream at the hub and tip of the blade, and reduce it on the midspan region. This can be observed from the pitchwise averaged values of the mass flow density in figure 4.7.

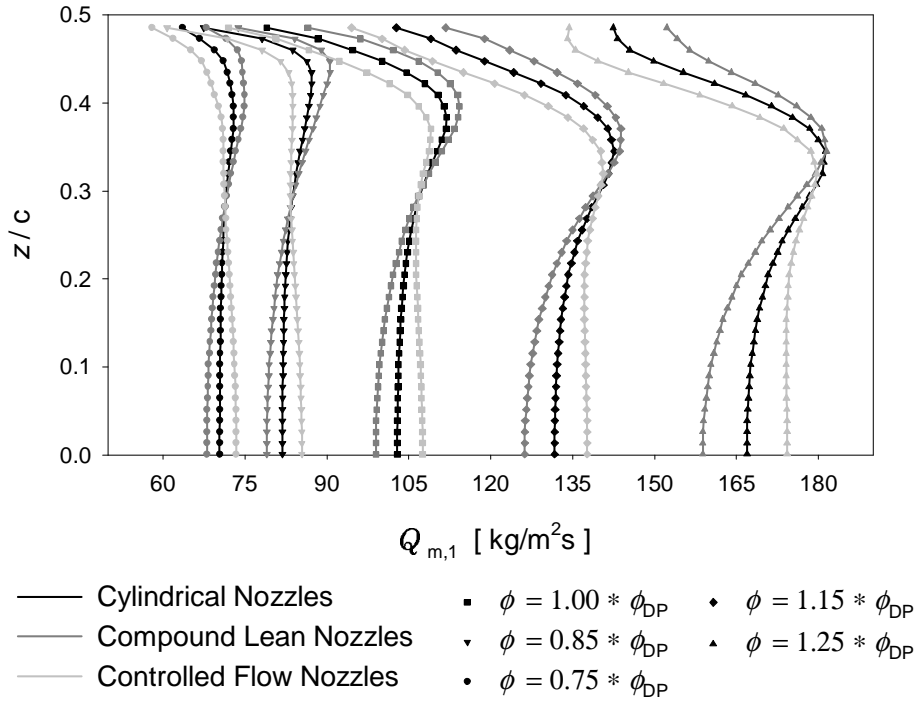


Fig. 4.7: *Pitchwise mass flow density at the plane 3.*

While examining the off-design behavior, it is noticeable how the peak in the mass flow density is changing its position with the change of the flow coefficient. The increase of the flow coefficient moves the peak further away from the endwall and also increases the variation in the mass flow distribution in the pitchwise direction. At part load, the variation decreases and the distribution is mainly affected by the endwall boundary layer. The importance of the mass flow density distribution rises while examining the losses.

Naturally, decreased mass flow density is preferred in the region where the losses are higher.

4.3 Inhomogeneity of the outlet flow field

Even though this method is used mainly for the optimization of the blade shapes, it provides an additional way to examine the outlet flow field of the cascade. The method is based on the Kreitmeier averaging method and it describes the inhomogeneity of the flow field. The inhomogeneity $\Delta\dot{K}$ is described as the difference of the irreversibly averaged kinetic energy K_{irr} and the reversibly averaged kinetic energy K_{rev} :

$$\Delta\dot{K} = \dot{K}_{irr} - \dot{K}_{rev} \quad (4.14)$$

The reversible averaging method does not allow any conversion of kinetic energy into thermal energy or vice versa over the mixing process. Thus, the kinetic energy remains constant over the mixing process. The reversibly averaged kinetic energy \dot{K}_{rev} is equal to the kinetic energy at the inlet of the control volume of the mixing process. Contrarily the irreversible averaging method allows a conversion of kinetic energy into thermal energy over the mixing process (Kreitmeier, 1977).

The values for the $\Delta\dot{K}$ for different nozzles at off-design conditions are presented in figure 4.8. The higher the value of $\Delta\dot{K}$ the less homogenous is the flow field.

In figure 4.8 it is visible how the controlled flow nozzles have a higher inhomogeneity in the cases examined. This is due to the spanwise variation in the stagger angle. It is visible that on the differences in the inhomogeneity become insignificant at part load and that the flow field is more uniform than in the design point. At over load, the differences become greater. The controlled flow nozzles have higher inhomogeneity compared to the cylindrical nozzles. Compound lean nozzles make a significant difference to the cylindrical nozzles only for $\phi_{DP}/\phi = 1.25 \cdot \phi_{DP}$.

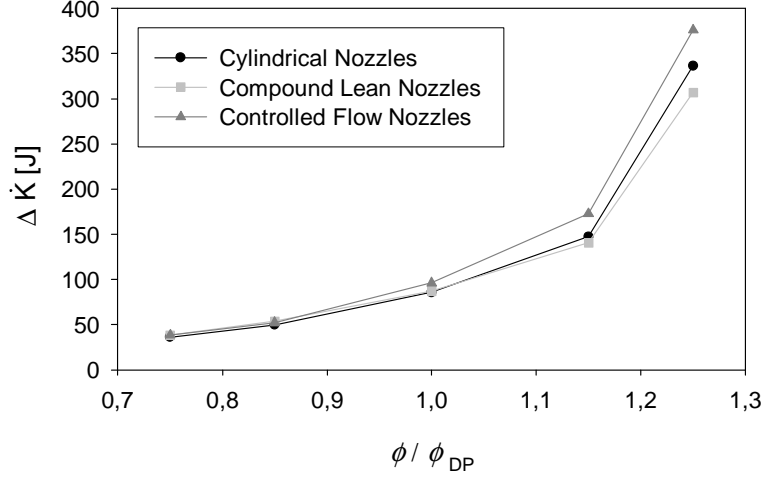


Fig. 4.8: *Flow field inhomogeneity at the plane 3.*

4.4 Outlet flow angle

As a part of the uniformity of the flow, it is useful to investigate the distribution of the outlet flow angles. Depending on the design of the rotor row, a certain outlet flow angle is preferred. As in this study there is no rotor row included, only the variation in the outlet flow angle is investigated. The outlet flow angle is calculated from the values in plane 3, and pitchwise averaged values are used to give a distribution along the blade height. The outlet flow angle α_1 is defined as

$$\alpha_1 = \arctan\left(\frac{c_x}{c_y}\right), \quad (4.15)$$

with respect to the circumferential direction. The outlet flow angle distributions for the investigated flow conditions are illustrated in figure 4.9.

In figure 4.9 it is visible how the controlled flow nozzles have a smaller exit angle in the vicinity of the endwall, compared to other nozzles. This is due to the twisting of the blade profiles, which results in a 2 degrees smaller stagger angle with respect to other nozzles. At midspan the difference in the stagger angle is +1 degree. This can be observed in the outlet flow angle near the midspan. The variations of the outlet flow angles in the range of $z/h=0.2-0.5$ is the result of the passage vortex and the trailing edge vortices. At low part load in example when the flow coefficient corresponds to $0.75 \cdot \phi_{DP}$, the vortices have almost no influence on the outlet flow angle.

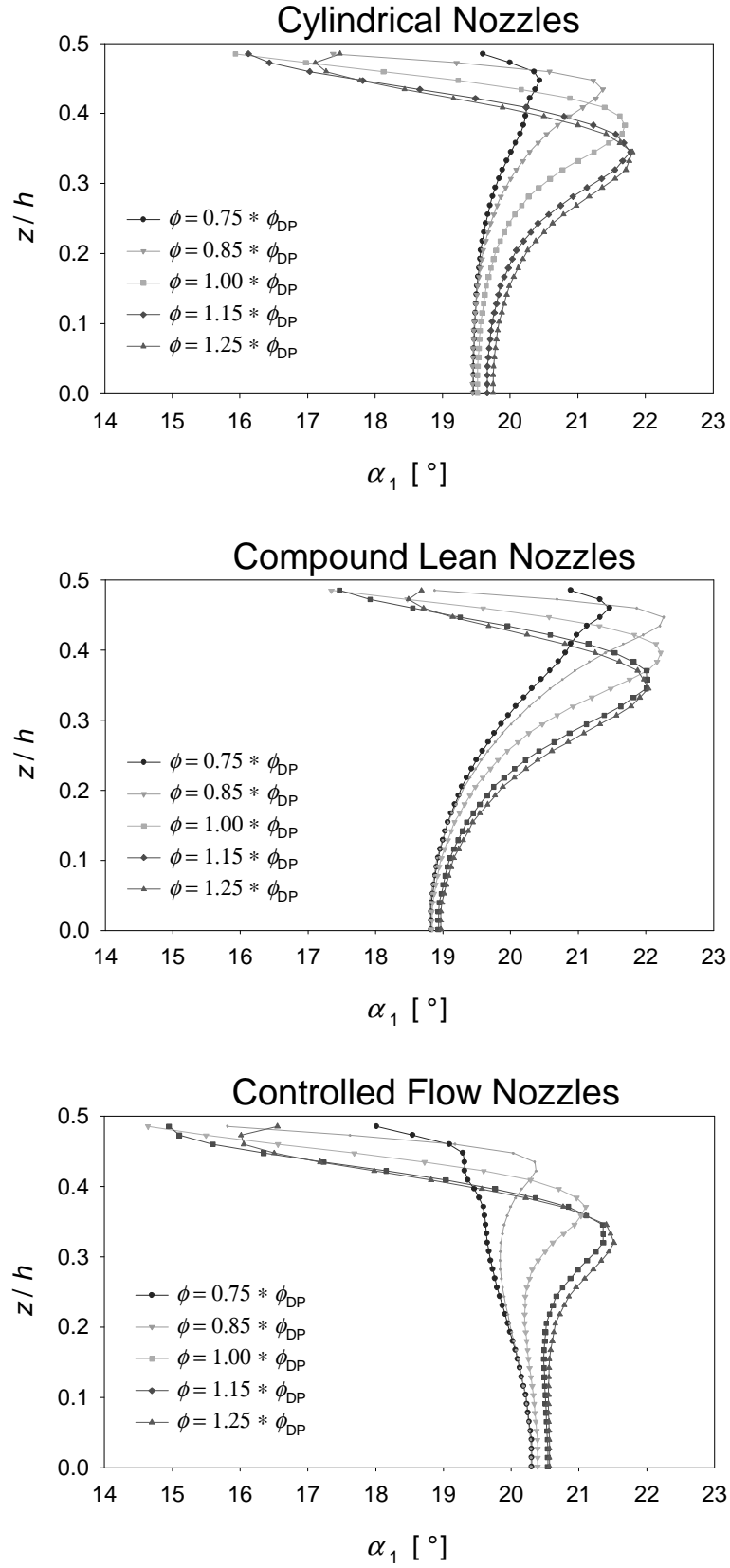


Fig. 4.9: *Outlet angles of the nozzles at plane 3.*

4.5 The total pressure loss

In an adiabatic flow, the losses consists of dissipation of kinetic energy due to viscous and mixing effects in the flow. This can be observed as a local decrease in the total pressure. Therefore, it is noted as the total pressure loss. The pressure loss coefficient ω is the difference between the total pressure at the inlet and outlet flow of the cascade, related to the dynamic pressure at the outlet.

The total pressure loss coefficient ω for compressible flow is defined as

$$\omega = \frac{p_{t0} - p_{t1}}{p_{t1} - p_1}, \quad (4.16)$$

where the total pressure is calculated by

$$p_t = \left[p^{-\frac{1}{\kappa}} \left(p + \rho \frac{(\kappa - 1)}{2 \kappa} c^2 \right) \right]^{\frac{\kappa}{\kappa - 1}}. \quad (4.17)$$

$\kappa = 1.4$ is the ratio of the specific heats for air.

In figure 4.10 the total pressure loss coefficient is illustrated as function of the flow coefficients.

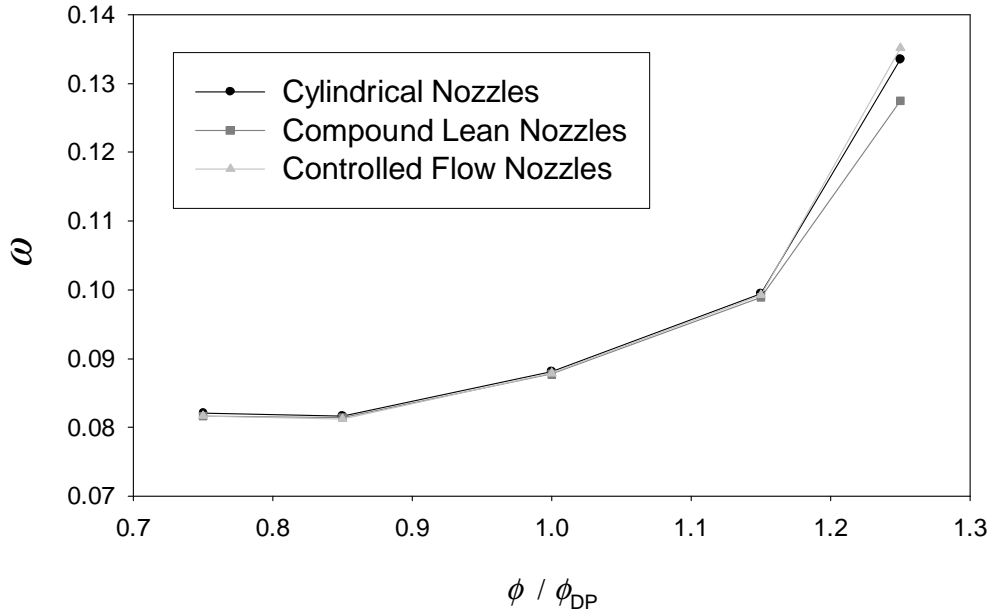


Fig. 4.10: *Total pressure loss coefficient.*

The differences between the nozzles rise at high over load ($\phi/\phi_{DP} = 1.25$) where the *compound lean nozzles* have lower losses. For all other investigated flow conditions there is no significant difference of the averaged total pressure loss coefficient.

4.5.1 Spanwise distribution of the total pressure losses

In order to investigate the differences in the spanwise distribution of the losses, the total pressure loss coefficient has to be calculated as function of the spanwise coordinate. Therefore, equation 4.16 is redefined to correspond to the pitchwise averaging:

$$\omega_p = \frac{p_{t0,p} - p_{t1,p}}{p_{t1} - p_1}, \quad (4.18)$$

where the subscript p refers to the pitchwise averaged values.

The distribution in the design point $\phi = \phi_{DP}$ and at high over load ($\phi/\phi_{DP} = 1.25$) is illustrated in figure 4.11

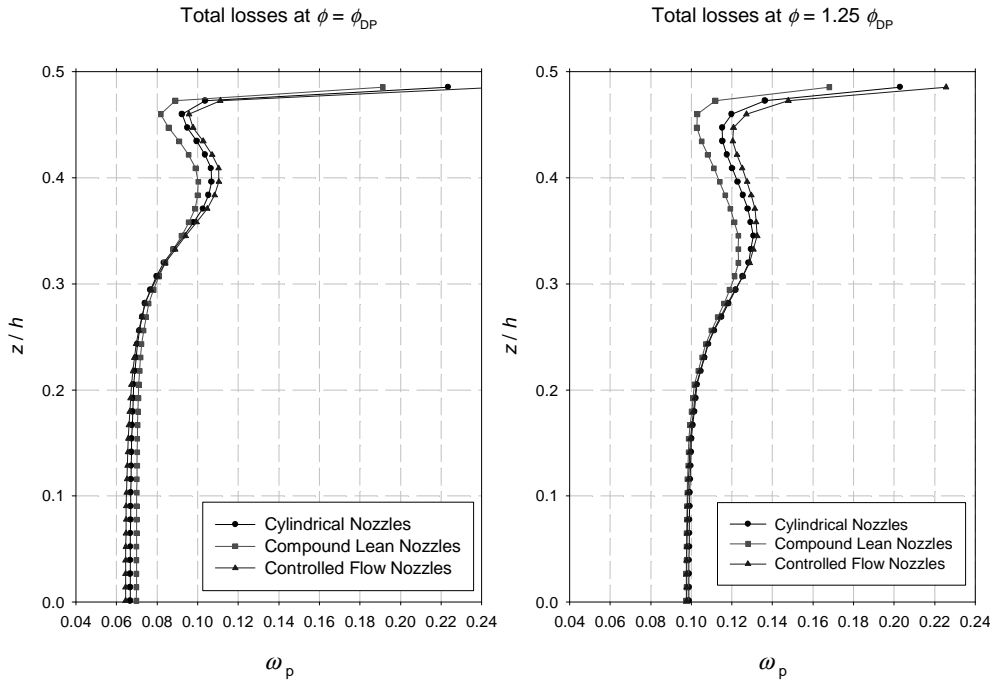


Fig. 4.11: *Pitchwise averaged total pressure loss coefficients.*

By comparing the two trends in figure 4.11, it can be seen that compared to the other two nozzles the compound lean nozzles have lower losses close to

the endwall ($z/h = 0.3 - 0.5$) and higher losses at midspan. The difference in midspan losses become insignificant at high over load ($\phi/\phi_{DP} = 1.25$) and therefore the total losses are at high over load lower than these of the other two nozzles.

4.5.2 Total pressure loss countours

For visualizing the distribution of the losses the two flow conditions examined in the previous section, contours of the losses are created. The values for the contours are created in similar manner to equation 4.18, but instead of pitchwise averaged values, the averaged values of the extracted data are used. The resulting contour plots are illustrated in figure 4.12.

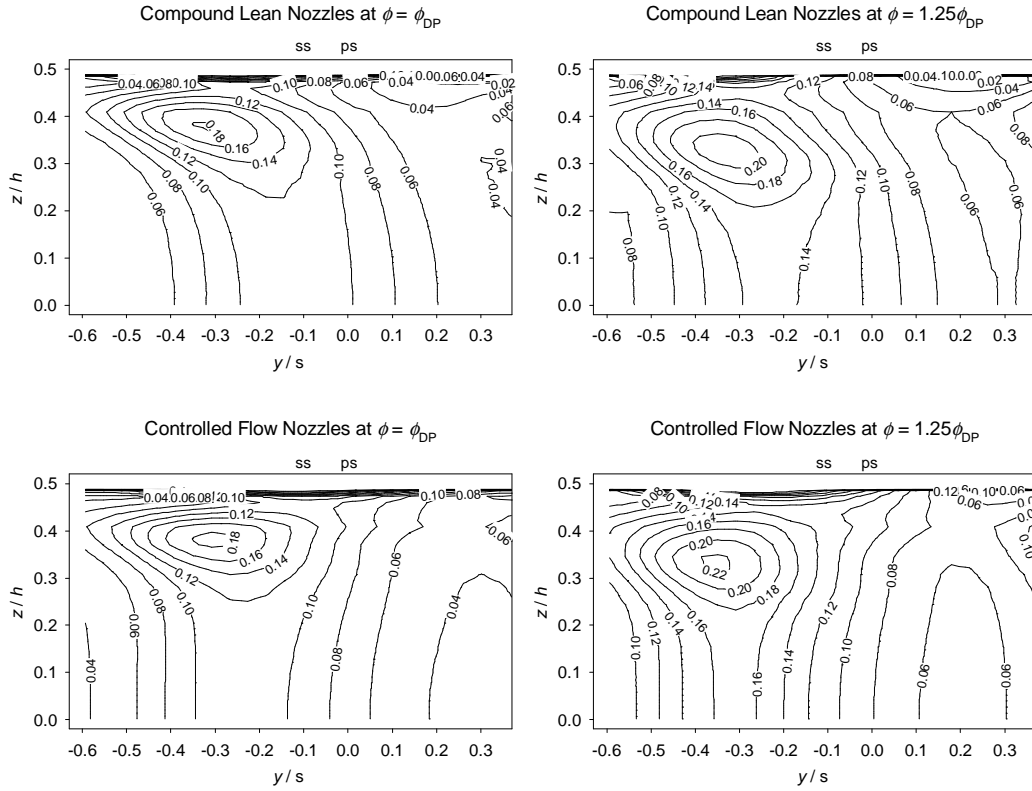


Fig. 4.12: *Total pressure loss coefficient contours.*

In figure 4.12 it is visible how the losses are distributed in the flow downstream of the compound lean and downstream of the controlled flow nozzles. The leaning of the blades of compound lean nozzles is clearly visible as bowed contouring. The straight trailing edges of the controlled flow nozzles prevent

this effect.

Comparing the loss cores with the location of the vortex centers in figures 4.4 and 4.6, it can be seen that they do not exactly coincide. The same behavior has been observed by other researchers (Gregory-Smith and Graves, 1983). The location of the loss cores is close to the center of the passage vortex, slightly shifted in the direction to the trailing edge vortex. The loss cores of the compound lean nozzles and controlled flow nozzles appear in the same location. The controlled flow nozzles have higher losses at the core than the compound lean nozzles, for both illustrated flow conditions. Near midspan the compound lean nozzles have lower losses in the wake than the controlled flow nozzles, but higher outside the wake.

4.6 Isentropic efficiency

The static-to-static isentropic efficiency is defined as:

$$\eta_s = \frac{\Delta h}{\Delta h_s}, \quad (4.19)$$

where Δh_s is the isentropic enthalpy drop over the cascade, which is defined as:

$$\Delta h_s = \frac{\kappa}{\kappa - 1} \frac{p_{t0}}{\rho_0} \left[\left(\frac{p_{t1}}{p_{t0}} \right)^{\frac{\kappa-1}{\kappa}} - 1 \right]. \quad (4.20)$$

The averaged isentropic efficiencies at different flow coefficients are illustrated in figure 4.13.

Compared to the design point at part load ($\phi/\phi_{DP} = 0.75 - 0.85$), the efficiency decreases slightly for all nozzles and no significant difference exists between the nozzles. Compared to the design point at the high over load ($\phi/\phi_{DP} = 1.25$), the drop in the isentropic efficiency is high. Also the differences between the nozzles are higher. The compound lean nozzles have the highest efficiency (0.878) and the efficiency of the reference cylindrical nozzles drops to a value of 0.862. The controlled flow nozzles have the lowest efficiency with a value of 0.857. With the respect to the design point, for

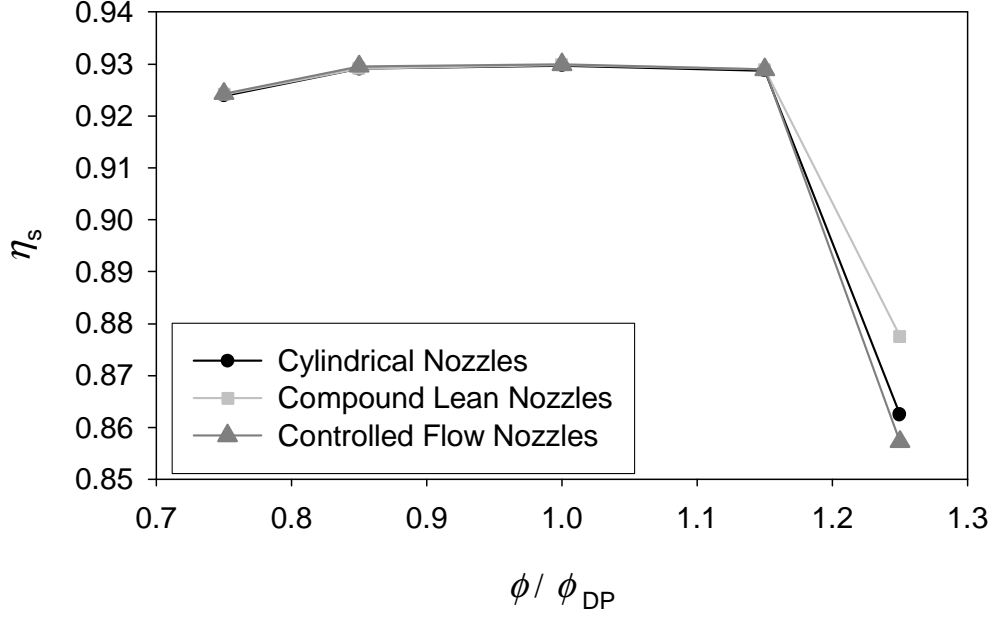


Fig. 4.13: *Isentropic efficiencies.*

($\phi/\phi_{DP} = 0.85, 1.15$) the drop in the isentropic enthalpy is less than 0.11 percentage unit of the design point value for all the nozzles.

4.7 Comparison of the results with measurements

Difficulties rise in finding suitable measurements to validate the obtained results. There exists vast amount of measurements for axial turbines, with different nozzle geometries. Finding measurements that have the same flow conditions as in the ERCOFTAC test-case creates problems. In the work of Zeschky (1991) the geometry of the stator blades is the same as that of the cylindrical nozzles and the flow conditions are similar to the design point.

In figure 4.14, are illustrated the axial velocity component and the outlet flow angle from the measurements of Zeschky (1991) and from the simulation with cylindrical nozzles at the design point. The measurements of Zeschky (1991) correspond to the location of plane 2 in the simulations (see fig. 2.7). The cascade of Zeschky (1991) was an annular one, which naturally affects the flow field. The results may be compared qualitatively, as the flow conditions are similar.

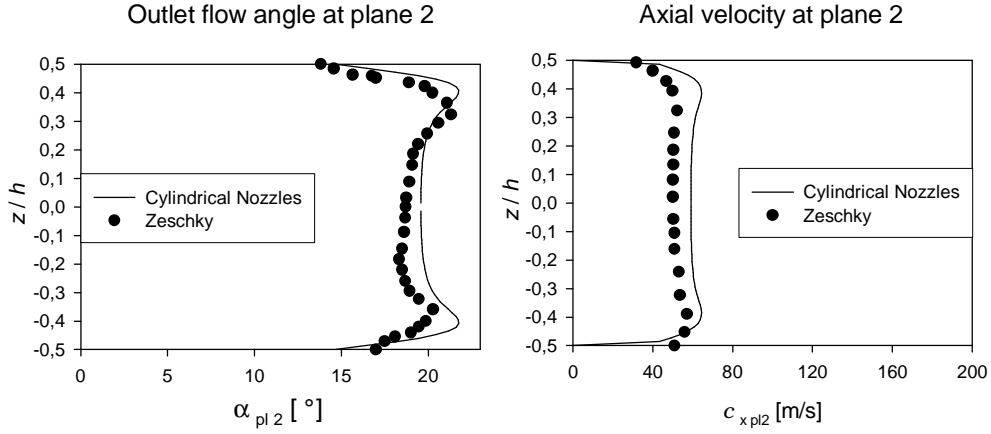


Fig. 4.14: Comparison of the obtained results with measurements by Zeschky (1991).

The comparison with the outlet flow angle shows how the annular cascade affects the flow. According to the simplified sine rule, the outlet flow angle is mainly affected by the geometry. But there are also influences by different flow conditions. The differences of the results from the measurements of Zeschky (1991) and from the simulation can be explained partly with the annular respect to linear cascade. The annular cascade invokes a pressure gradient working in spanwise direction from shroud to hub. This strengthens the passage vortices and therefore the peak in the outlet flow angle distribution is further away from the endwalls than for the linear cascade. The smaller angle at midspan of the annular cascade can be explained with the vortex that originates by the non-equilibrium in the wake. Therefore, secondary velocity components in the circumferential direction are originated and the outlet flow angle is lowered.

Chapter 5

Conclusions and discussion

The differences in the nozzle's performances are small, except at high over load ($\phi = 1.25 \cdot \phi_{DP}$). The main reason for the small differences is the similarity of the geometries. The optimized geometries do not differ much from each other and therefore big differences cannot be expected.

5.1 Losses

The overall total pressure losses are similar for all nozzles, except at high over load ($\phi = 1.25 \cdot \phi_{DP}$). There the compound lean nozzles have lower overall losses than the controlled flow nozzles.

The comparison of the spanwise distribution of the pressure losses shows that the losses are formed in different sections of the nozzles. Compared to the other nozzles, the compound lean nozzles have higher losses close to midspan and lower losses close to the endwall. For the investigated nozzles the differences in the losses close to midspan are smaller at high over load. Therefore, the compound lean nozzles perform better than the other nozzles.

The difference between the controlled flow nozzles and the compound lean nozzles may be originated by the secondary losses. The separation of the losses was not possible, so this cannot be confirmed, but as the differences appear near the endwall where most of the secondary losses are created, this assumption is reasonable.

5.2 Inhomogeneity of the outlet flow field

It was shown for all the nozzles that the inhomogeneity of the outlet flow field is higher at over load. At part load, the outlet flow field become more homogenous, but the difference compared to the design point was smaller than at over load. The controlled flow nozzles have a less homogenous flow field, especially at the design point and at over load. This might be caused by the variation in the stagger angle, which also causes differences in the outlet flow angle. At part load the differences become insignificant.

5.3 Secondary flow and vortices

The vorticity and the secondary flows increase with the flow coefficient. The passage vortex appears downstream of all the nozzles, but strongest downstream of the controlled flow nozzles. Also the cross-flow near the endwall appears strongest downstream of the controlled flow nozzles. The compound lean nozzles have a weaker cross-flow compared to the cylindrical nozzles.

Downstream of the compound lean nozzles and the cylindrical nozzles the trailing edge vortices appear clearly as one big vortex. Downstream of the controlled flow nozzles this vortex is not so clear as downstream of the other two nozzles.

5.4 Massflow density

The compound lean nozzles direct more massflow near the endwall than the other nozzles. The controlled flow nozzles direct the massflow from the areas where the losses are generated, to the midspan region.

5.5 Isentropic efficiency

The differences in the isentropic efficiency between the nozzles are moderate in all cases except at the high overload ($\phi/\phi_{DP} = 1.25$). There, the controlled

flow nozzles have a much lower isentropic efficiency than the compound lean nozzles. At part load the isentropic efficiency do not drop much below the design point value for all the nozzles.

5.6 Summary

It was found in the study that the moderate ($\phi/\phi_{DP} = \pm 0.15$) off-design conditions do not cause significant drop the performance of the investigated nozzles. The major differences are encountered at high over load ($\phi/\phi_{DP} = 1.25$), where the compound lean nozzles suffers less loss in efficiency than the controlled flow nozzles and the reference cylindrical nozzles. In order to confirm the results obtained by the numerical simulation, experimental results should be conducted.

Bibliography

- [1] CFX-4 Solver manual, 1997. CFX-4.2: Solver manual. CFX International, AEA Technology. Harwell, Didcot, Oxfordshire.
- [2] Fluent Inc., 1993. Introduction to the Renormalization Group Method and Turbulence Modelling. Fluent Inc. Lebanon, NH 03766. TM-107. Technical Memorandum.
- [3] Gregory-Smith D., 1996. Physics of secondary flows. Secondary and tip-clearance flows in axial turbomachines. VKI Lecture Series 1997 - 01.
- [4] Haller B., 1996. Full 3D turbine blade design. VKI Lecture Series 1997 - 01.
- [5] Harrison S., 1992. The influence of blade lean on turbine losses. Journal of Turbomachinery. Vol. 114, pp. 184.
- [6] Lakshminarayana B., 1996. *Fluid Dynamics and Heat Transfers of Turbomachinery*. John Wiley and Sons Inc, New York. ISBN 0-471-85546-4.
- [7] Langston L., 2001. Secondary flows in axial turbomachines - a review. Annals of the New York Academy of Sciences. Heat Transfer in Gas Turbine Systems. Vol. 934 , pp. 26.
- [8] Gardzilewicz A., Lampart P., 1999. Numerical study of 3d blading in HP impulse turbines. Ciepłne Maszyny Przepływowe. Vol. 115, pp. 297 - 310.
- [9] Kreitmeier F., 1977. Integralbehandlung inhomogener Strömungsfelder, Teilbericht 1: Theorie. ABB Baden, Switzerland. Technical paper.

- [10] Küttner K., Beitz W., 1990. *Dubbel, Taschenbuch für den Maschinenbau, 17th edition*. Springer-Verlag, Berlin, Heidelberg, New York. ISBN 3-540-52381-2.
- [11] Langston L., Eckerle A., 1986. Horseshoe vortex formation around a cylinder. Asme. 86-GT-246. pp.9.
- [12] Müller K., Willinger R., 2000. Vorlesung über Grundzüge der thermischen Turbomaschinen. Institut für Thermische Turbomaschinen und Energieanlagen. Technische Universität Wien.
- [13] Schiebenes A., 2001. Rechnerischer Vergleich von Compound Lean Nozzles mit Controlled Flow Nozzles. Universität Stuttgart. Master's thesis.
- [14] Schlichting, H., 1979 Boundary-layer theory, 7th edition. McGraw-Hill. New York. ISBN 0-07-055334-3.
- [15] Siikonen, T., 2001. Laskennallisen virtausmekaniikan ja lämmönsiirron perusteet. Helsinki University Of Technology.
- [16] Sieverding C. H., 1985. Recent progress in an understanding of basic aspects of secondary flow in turbine blade passage. Journal of Engineering of Gasturbines and Power. Vol. 107, pp. 248 - 257.
- [17] Xu J. D., Denton L., 1999. The exploitation of 3-D flow in turbomachinery design. VKI Lecture Series 1999-02. pp. 121.
- [18] Walraevens R., 2000. Experimentelle Analyse dreidimensionaler instationär Strömungseffekte in einer 1-1/2-stufigen Axialturbine. Fortschritt-Berichte VDI. Reihe 7, Nr. 385. pp. 294.
- [19] Wei N., 2002. Significance of Loss Models in Aerothermodynamic Simulation for Axial Turbines. Kungliga Tekniska Högskolan, Stockholm. PhD-thesis.
- [20] White F., 1991. Viscous Fluid Flow, 2nd ed. McGraw-Hill, New York. ISBN 0-07-069712-4.
- [21] Wingelhofer F., 2003. Neue Kriterien zur Auslegung dreidimensionaler Beschaukelungen von Axialturbinen. Technische Universität, Wien. PhD-thesis.

- [22] Zeschky J., 1991. Experimentelle Untersuchung der dreidimensionalen instationären Rotorströmung einer axialen Kaltluftturbine. RWTH Aachen, Germany. PhD-Thesis.

Appendix A

Example of the command file for CFX-4

The example command file below was used to run the simulation for the cylindrical nozzles at design point.

```
>>CFX4
  >>OPTIONS
    THREE DIMENSIONS
    BODY FITTED GRID
    UNMATCHED GRIDS
    CARTESIAN COORDINATES
    TURBULENT FLOW
    HEAT TRANSFER
    COMPRESSIBLE FLOW
    STEADY STATE
    USER SCALAR EQUATIONS 3
  >>USER FORTRAN
    USRBCS
    USRGRD
    USRPRT
    USRWRK
    USRDMP
  >>VARIABLE NAMES
    USER SCALAR1  'YPLUS'
    USER SCALAR2  'YAW ANGLE'
    USER SCALAR3  'EPSILON LOG RES'
    U VELOCITY 'U VELOCITY'
    V VELOCITY 'V VELOCITY'
    W VELOCITY 'W VELOCITY'
    PRESSURE     'PRESSURE'
    K 'K'
    EPSILON 'EPSILON'
```

```

    TEMPERATURE 'TEMPERATURE'

>>MODEL TOPOLOGY
  >>CYCLIC CONNECTIONS
    Y CYCLE LENGTH 0.0478
  >>GLUE PATCHES FOR UNMATCHED GRIDS
    FIRST PATCH NAMES 's_side_per'
    SECOND PATCH NAMES 'p_side_per'

>>MODEL DATA
  >>DIFFERENCING SCHEME
    ALL EQUATIONS 'HYBRID'
  >>SET INITIAL GUESS
    >>INPUT FROM FILE
      READ DUMP FILE
      LAST DATA GROUP
      END
  >>RHIE CHOW SWITCH
    IMPROVED
    LINEAR EXTRAPOLATION
    MULTIPHASE DAMPING
    MODIFIED RESISTANCE TREATMENT
    HARMONIC AVERAGING OF COEFFICIENTS
  >>TITLE
    PROBLEM TITLE 'CYL BLADES,COMPRESSIBLE,TURBULENT-RNG'
  >>WALL TREATMENTS
    WALL PROFILE 'LOGARITHMIC'
    NO SLIP
  >>PHYSICAL PROPERTIES
    >>SCALAR PARAMETERS
      >>DIFFUSIVITIES
        ALL USER SCALARS 1.0
    >>FLUID PARAMETERS
      VISCOSITY 1.52600E-05
    >>HEAT TRANSFER PARAMETERS

```

```

THERMAL CONDUCTIVITY          0.02603
FLUID SPECIFIC HEAT           1007.0
ENTHALPY REFERENCE TEMPERATURE 273.15
>>COMPRESSIBILITY PARAMETERS
FULLY COMPRESSIBLE
UNIVERSAL GAS CONSTANT      8314.00
FLUID MOLECULAR WEIGHT       28.79
REFERENCE PRESSURE          101300.0
MINIMUM REAL PRESSURE       100000.0
MINIMUM TEMPERATURE         273.15
HIGH MACH NUMBER SIMPLE ALGORITHM
>>TURBULENCE PARAMETERS
>>TURBULENCE MODEL
TURBULENCE MODEL 'RNG K-EPSILON'

>>SOLVER DATA
>>PROGRAM CONTROL
MAXIMUM NUMBER OF ITERATIONS 1
MAXIMUM CPU TIME 1000000
MASS SOURCE TOLERANCE 1.0000E-06
ITERATIONS OF TURBULENCE EQUATIONS 2
ITERATIONS OF VELOCITY AND PRESSURE EQUATIONS 2
ITERATIONS OF TEMPERATURE AND SCALAR EQUATIONS 2
ITERATIONS OF HYDRODYNAMIC EQUATIONS 1
>>DEFERRED CORRECTION
K START          100
K END            1000
EPSILON START    100
EPSILON END      1000
>>EQUATION SOLVERS
U VELOCITY 'BLOCK STONE'
V VELOCITY 'BLOCK STONE'
W VELOCITY 'BLOCK STONE'
PRESSURE   'BLOCK STONE'
K          'BLOCK STONE'

```

```

    EPSILON      'BLOCK STONE'
    ENTHALPY     'BLOCK STONE'
>>PRESSURE CORRECTION
    SIMPLEC
>>REDUCTION FACTORS
    U VELOCITY 2.5000E-01
    V VELOCITY 2.5000E-01
    W VELOCITY 2.5000E-01
    PRESSURE 1.000E-01
    K 2.5000E-01
    EPSILON 2.5000E-01
>>UNDER RELAXATION FACTORS
    U VELOCITY 0.55
    V VELOCITY 0.55
    W VELOCITY 0.55
    K          0.55
    EPSILON    0.55
    ENTHALPY   0.55

>>CREATE GRID
>>INPUT GRID
    READ GRID FILE
    END

>>MODEL BOUNDARY CONDITIONS
>>INLET BOUNDARY CONDITIONS
    VELOCITY SPECIFIED
>>INLET BOUNDARIES
    PATCH NAME 'Inlet'
    TURBULENCE INTENSITY 2.0000E-02
    DISSIPATION LENGTH SCALE 4.7800E-05
    TEMPERATURE 304.41
    U VELOCITY 51.878
    V VELOCITY 0.0
    W VELOCITY 0.0

```



```
>>PRESSURE BOUNDARIES
    PATCH NAME 'Outlet'
    PRESSURE 4.518E+04
    STATIC PRESSURE SPECIFIED
>>WALL BOUNDARIES
    PATCH NAME 'profile'
    PATCH NAME 'walls'
>>OUTPUT OPTIONS
>>DUMP FILE OPTIONS
    ALL VARIABLES
    GEOMETRY DATA
    FINAL SOLUTION
>>LINE GRAPH DATA
    RESIDUAL
    EACH ITERATION
    FILE NAME 'RESIDUAL.RES'
    U VELOCITY
    V VELOCITY
    W VELOCITY
    PRESSURE
    DENSITY
    VISCOSITY
    K
    EPSILON
    ENTHALPY
    YPLUS
>>STOP
```